Engineering Structures 322 (2025) 119040

Contents lists available at ScienceDirect

Engineering Structures

journal homepage: www.elsevier.com/locate/engstruct

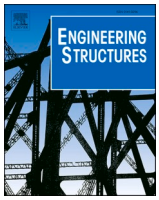

Experimental and analytical investigation of the crack behaviour of dapped-end beams

Jaime Mata-Falcón [a,1], Karin L. Yu [b,*,1], Luis Pallarés Rubio [c], Pedro Miguel Sosa [c]

[a] Department of Mechanics of Continuous Media and Theory of Structures, Universitat Politècnica de València, Valencia, Spain
[b] Institute of Structural Engineering and ETH AI Center, ETH Zurich, Zurich, Switzerland
[c] Institute of Concrete Science and Technology, Universitat Politècnica de València, Valencia, Spain

ARTICLE INFO

Keywords:
Concrete structures
Dapped-end beams
Experimental study
Strut-and-tie models
Service behaviour
Crack behaviour
Bond behaviour
Digital image correlation

ABSTRACT

Reinforced concrete dapped ends are a widely used connection for precast elements in infrastructure and building structures. However, they are prone to major durability problems due to the formation of an inclined crack at the re-entrant corner of the joint. The crack typically forms at low loads and reaches a significant opening under service load conditions, causing corrosion and stress concentration in the reinforcement, which impairs the safety of the connection. The behaviour of these cracks in a highly disturbed structural region is not well understood. This paper presents the experimental results of 28 dapped-end tests in which the crack behaviour in the re-entrant corner was continuously measured using digital image correlation. The main test variables are the amount of dapped-end reinforcement, the presence of diagonal reinforcement and the ratio of horizontal to vertical dapped-end reinforcement area. The bond behaviour of the dapped-end reinforcement was estimated from the measured crack widths and reinforcement strains, assuming a pull-out mechanism with constant bond shear stresses on both crack sides. The paper proposes a model for evaluating the width of corner cracks at service loads, in which the reinforcement strains are derived from strut-and-tie models. The modelling results agreed satisfactorily well with the experimental observations of this study and 28 additional tests from the literature for dapped-ends with reinforcement diameter below 20 mm.

1. Introduction

Reinforced concrete dapped ends, also commonly known as Gerber joints or half-joints, are a widely used connection for precast elements (see an example in Fig. 1). Dapped ends were extensively used in bridges in the second half of the 20th century due to the simplicity of the hinged expansion joint. On the UK Highways England road network alone, there were 424 bridges built with dapped ends as of 2018 [1]. This type of connection is still frequently used in building structures to link a beam and a corbel, while keeping the depth of the structure constant. In a dapped end, the load is applied at the nib (i.e. reduced depth section) and transferred to the full section beam. This distinctive force flow around a depth discontinuity induces a strong stress concentration around the re-entrant corner, which triggers the formation of a diagonal crack at low loads. The crack forming at the re-entrant corner reaches a significant opening under service load conditions, typically exceeding the serviceability limits specified in design codes [2,3]. This causes durability issues, particularly due to corrosion of the main reinforcement of the joint in bridges exposed to de-icing salts. Desnerck et al. found that approximately 50% of the Gerber type bridges analysed showed significant deterioration and structural problems in the dapped-end connections [1]. Corrosion and poor detailing of dapped-end connections contributed to the collapse of bridges in Canada and Italy [4,5].

The failure behaviour of dapped-end beams has been studied extensively in the past, both experimentally and analytically [6–14]. The connections are typically designed in the ultimate state using plastic approaches. Strut-and-tie models are the most common design option, as they allow for the proper detailing of structural elements based on the flow of forces [15,16]. The use of kinematic-based approaches tailored to the particularities of the connections has also shown good application [12,17]. Moreover, numerical methods such as nonlinear finite element analyses have been used to validate analytical models or predict the failure responses of dapped-end beams [18,19]. On the other hand, the

* Correspondence to: ETH Zurich, Stefano-Franscini-Platz 5, 8093 Zurich, Switzerland.
E-mail address: karin.yu@ibk.baug.ethz.ch (K.L. Yu).
[1] Both authors contributed equally to this work and should be regarded as co-first authors

https://doi.org/10.1016/j.engstruct.2024.119040

Available online 7 October 2024
0141-0296/© 2024 The Authors. Published by Elsevier Ltd. This is an open access article under the CC BY license (http://creativecommons.org/licenses/by/4.0/).

Fig. 1. Reinforced concrete dapped-end connection: overpass in road CV-500 near Valencia with deterioration due to diagonal crack at the re-entrant corner and poor state of the joint sealant.

behaviour of the diagonal cracks originating at the re-entrant corner is not yet well understood, even though the control of such cracks at service loads usually governs the overall design of dapped ends. Only a few experimental campaigns have reported the crack behaviour of dapped-end beams in detail [9,11–13,20].

The behaviour of the crack forming at the re-entrant corner differs significantly from the behaviour of distributed cracks due to bending or tension. On the one hand, the diagonal crack forms at very low loads due to the concentration of tensile stresses around the re-entrant corner. Therefore, the crack is initially isolated until secondary cracks may appear in the vicinity of the joint at higher loads [21]. This requires the development of models that consider a single crack within a stress concentration region. On the other hand, the crack forms in a highly disturbed region, which invalidates conventional approaches to estimate reinforcement strains based on cross-sectional approaches [2]. Recently, several approaches have been proposed to calculate the crack width in dapped-end beams [11,21,22]. However, there is a high uncertainty in the bond strength to be considered for the dapped-end reinforcement. While for distributed cracks in tension chords the bond is typically assumed to be approximately twice the mean concrete tensile strength in the elastic region [23], Rajapakse found that this bond strength had to be significantly reduced for dapped ends to obtain reasonable crack width predictions using a kinematic-based analysis [22]. The empirical bond fitted by Rajapakse varied between 15% and 50% of the standard value in tension chords depending on the amount and diameter of reinforcement, indirectly accounting for characteristic phenomena near the re-entrant corner of the dapped end such as biaxial tension, micro- and macrocracking and restrained shrinkage. Despite the uncertainty of the bond strength for dapped-end reinforcement and its large influence on crack width verification, this mechanical property has not been directly quantified until now.

To contribute to the limited knowledge of the service behaviour of dapped-end beams, this paper investigates the bond and crack behaviour of dapped ends in an experimental campaign consisting of 28 three-point bending tests. The crack width and reinforcement strains are continuously monitored to quantify the bond strength of the dapped-end reinforcement, assuming a pull-out mechanism with constant bond shear stresses on both crack sides. Based on the experimental observations, a model is proposed to estimate the width of the crack forming at the re-entrant corner of the dapped end. The model is based on the bond shear stresses estimated from the experimental observations and the reinforcement strains obtained from a strut-and-tie model that takes into account the peculiarities of the dapped end at service loads. In the last section of the paper, the model is validated against the experimental results of this study and other studies from the literature.

2. Experimental campaign

The structural behaviour of dapped ends with different reinforcement amounts and configurations was investigated in an experimental campaign comprising 28 dapped-end tests belonging to 15 beam specimens. The crack and bond behaviour of the reinforcement around the re-entrant corner was studied in detail using continuous digital image correlation (DIC) measurements on the surface and strain gauges glued on the steel bars. More information on the test series, including their ultimate behaviour, can be found elsewhere [7,24].

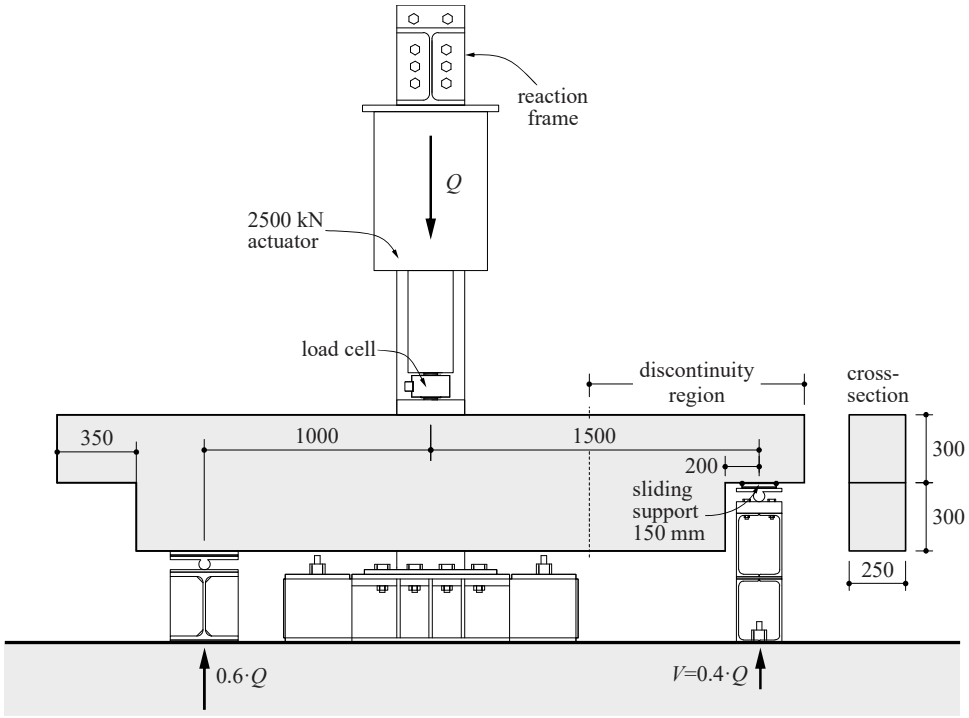

Fig. 2. Test setup and geometry of the dapped-end beams (dimensions in [mm]).

Table 1
Graphical description, reinforcement definition and concrete cylindrical compressive strength of the beam specimens.

		Dapped-end reinforcement					Beam reinforcement			
Specimen (reinf. layout)	**Graphical description**[+]	$A_{s,H}$ (mm^2)	$A_{s,V1}$ (mm^2)	$A_{s,V2}$ (mm^2)	$A_{s,V3}$ (mm^2)	$A_{s,D}$ (mm^2)	$A_{s,F1}$ (mm^2)	$A_{s,F2}$ (mm^2)	$A_{s,T}$ (mm^2/m)	f_c [MPa]
DEB-1.1 (O.1)	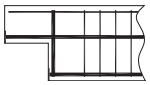	5Ø10 (393)	2Ø10 + 2Ø8 (258)	-	-	-	4Ø20 (1257)	-	2Ø8/0.125 (808)	41.1
DEB-1.2 (O.2)	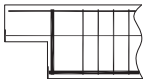	3Ø10 (236)	2Ø10 + 2Ø8 (258)	-	-	-	4Ø20 (1257)	-	2Ø8/0.125 (808)	39.3
DEB-1.3 (O.3)	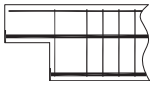	5Ø10 (393)	2Ø8 (101)	-	-	-	4Ø20 (1257)	-	2Ø8/0.125 (808)	39.9
DEB-1.4 (O.1)	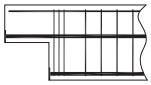	5Ø10 (393)	2Ø8 (101)	2Ø6 (57)	2Ø8 (101)	-	4Ø20 (1257)	-	2Ø8/0.125 (808)	40.4
DEB-1.5 (O.2)	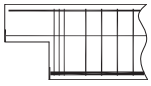	3Ø10 (236)	2Ø8 (101)	2Ø6 (57)	2Ø8 (101)	-	4Ø20 (1257)	-	2Ø8/0.125 (808)	40.8
DEB-1.6 (O.1)	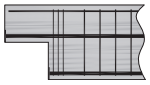	4Ø16 (804)	2Ø10 (157)	2Ø12 (226)	2Ø10 (157)	-	4Ø25 (1963)	4Ø16 (804)	4Ø8/0.125 (1608)	31.1
DEB-1.7 (O.2)	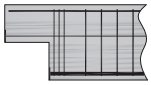	4Ø12 (452)	2Ø10 (157)	2Ø12 (226)	2Ø10 (157)	-	4Ø25 (1963)	4Ø16 (804)	4Ø8/0.125 (1608)	30.0
DEB-1.8 (O.1)	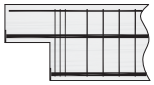	5Ø12 (565)	2Ø10 (157)	2Ø6 (57)	2Ø10 (157)	-	4Ø25 (1963)	-	2Ø8 + 2Ø6/0.125 (1256)	32.2
DEB-1.9 (O.2)	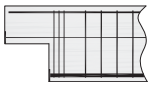	3Ø12 (339)	2Ø10 (157)	2Ø6 (57)	2Ø10 (157)	-	4Ø25 (1963)	-	2Ø8 + 2Ø6/0.125 (1256)	31.9
DEB-2.1 (D.1)	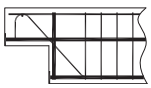	3Ø10 (236)	3Ø8 (151)	-	-	2Ø10 (157)	4Ø20 (1257)	-	2Ø8/0.125 (808)	40.2
DEB-2.2 (D.1)	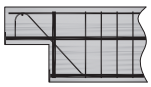	4Ø12 (452)	4Ø10 (314)	-	-	2Ø12 + 1Ø10 (305)	4Ø25 (1963)	4Ø16 (804)	4Ø8/0.125 (1608)	33.3
DEB-2.3 (D.1)	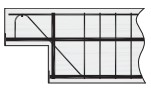	3Ø12 (339)	2Ø12 (226)	-	-	2Ø12 (226)	4Ø25 (1963)	-	2Ø8 + 2Ø6/0.125 (1256)	33.3
DEB-2.4 (D.2)	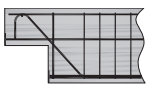	4Ø10 (314)	2Ø12 (226)	-	-	2Ø12 + 1Ø16 (427)	4Ø25 (1963)	4Ø16 (804)	4Ø8/0.125 (1608)	36.9
DEB-2.5 (D.3)	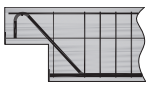	2Ø8 + 2Ø6 (157)	2Ø8 (101)	-	-	2Ø16 + 1Ø12 (515)	4Ø25 (1963)	4Ø16 (804)	4Ø8/0.125 (1608)	37.1
DEB-2.6 (D.4.1)	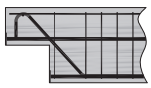	4Ø16 (804)	2Ø8 (101)	-	-	2Ø16 + 1Ø12 (515)	4Ø25 (1963)	4Ø16 (804)	4Ø8/0.125 (1608)	38.3

[+] Reinforcement sizes are not to scale. Dimensions represent only relative differences between specimens. The shading colour symbolises the amount of reinforcement as follows:

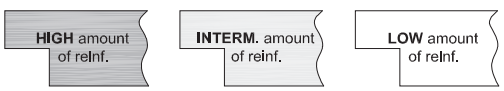

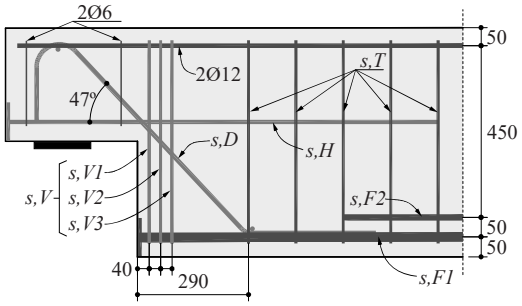

Fig. 3. Reinforcement notation and geometry (main reinforcement of the dapped end in light grey; dimensions in [mm]).

2.1. Specimens, materials and test setup

Fig. 2 shows the test setup and geometry of the beams. Each dapped end of the beam was tested independently with a non-symmetric three-point bending loading configuration. The beam specimens had a total length of 3300 mm with a rectangular cross-section of 250 × 600 mm, reduced to 250 × 300 mm at the dapped ends. The nib had a length of 350 mm. Both sides of the beam featured the same reinforcement configuration, resulting in twin tests. Table 1 provides the reinforcement layouts according to the graphical representation and nomenclature defined in Fig. 3. The horizontal and vertical mechanical concrete covers were 40 mm and 50 mm, respectively.

The beam specimens with the code DEB-1.X contained only orthogonal reinforcing bars in the dapped end, while those with the code DEB-2.X additionally included diagonal reinforcing bars at the re-entrant corner. The DEB-1.X series examined different layouts and ratios of horizontal and vertical reinforcement amounts at the re-entrant corner ($A_{s,H}/A_{s,V}$). Table 1 shows the codification of the reinforcement layout below the specimen codification. Layout O.1 is the reference configuration and is designed with a strut-and-tie model according to EN1992–1-1 [2], i.e. with $A_{s,H}/A_{s,V}$ of approximately 1.5. Layouts O.2 and O.3 consider an alternative detailing of the horizontal or vertical reinforcement resulting in $A_{s,H}/A_{s,V} \approx 0.9$ and 3.9, respectively. In addition to the ratio $A_{s,H}/A_{s,V}$, the reinforcement content also varied, as indicated by the shading colour of the graphical description for the beam specimens in Table 1. As a reference, the beams with the highest reinforcement content had roughly double the reinforcement amount than the ones with the lowest content.

The specimens with the code DEB-2.X provided diagonal reinforcing bars at an inclination of 47° in addition to orthogonal dapped-end reinforcement with $A_{s,H}/A_{s,V} \approx 1.5$ (similar to Layout O.1). Three layouts were used to study the effect of the relative contribution of the diagonal load-bearing mechanism. In Layout D.1, the diagonal dapped-end reinforcement was designed to resist approximately 40% of the total load at failure, while in Layouts D.2 and D.3, this contribution was raised to 60% and 80%, respectively. Beam DEB-2.6 had a special layout (D.4.1), which included a significantly higher amount of horizontal dapped-end reinforcement (five times) than Beam DEB-2.5 of Layout D.3. While Layout D.1 was tested for the three examined reinforcement contents, the other diagonal layouts were used only for the largest reinforcement amount.

A normal-strength concrete with a characteristic compressive strength of 30 MPa and a maximum aggregate size of 20 mm was used for all specimens. The concrete was supplied by a local concrete mixing plant. The beam specimens were cast in three batches, corresponding to the groupings in Table 2. The compressive strength of each beam was determined by testing two 150 mm × 300 mm cylinders on the same day as the dapped end tests (see results in Table 1). The comparison of the resulting mean concrete compressive strengths of the different specimens show certain scatter, which is more related to the strength differences between the batches than to the age of the concrete. Reinforcing bars with a nominal yield strength of 500 MPa and ductility class B were used. Table 2 gives the mechanical properties (yield stress, f_y, and tensile strength, f_u) of the reinforcement that were determined from two tensile tests per diameter and batch.

For the simply supported dapped-end beams with a 2500 mm span, three-point non-symmetric bending tests were conducted. A 2500 kN hydraulic actuator, located 1500 mm from the dapped end being tested, applied the load by imposing a controlled displacement rate of 0.25 mm/min. A system of polished 5 mm thick stainless steel and Teflon plates enabled the supports to move horizontally and rotate. To allow for uniform load distribution, neoprene (300 × 150 × 20 mm) was placed on top of the sliding system.

2.2. Instrumentation and post-processing

A load cell below the hydraulic actuator measured the applied load Q. This experimental campaign used two types of measurement techniques. Firstly, the reinforcement of the beam specimens was instrumented with up to 45 strain gauges (3 mm measuring length and 120 Ω resistance) per test, which allowed the measurement of the reinforcement strains relative to the beginning of the test. Secondly, photos of one side of the specimens were taken at 1 Hz for image control purposes, using Canon EOS 5D Mark II cameras (5616 × 3744 px) with Canon EF 85 mm lenses. The monitored field of view resulted in an approximate resolution of 0.09 mm/px. These images were post-processed with DIC techniques to track surface displacements and strains, from which the crack locations and displacements were extracted.

Within this study, only the strain measurements of the dapped-end reinforcement were analysed, for which the strain gauges were strategically installed close to the diagonal crack forming at the re-entrant corner. The strain measurements on different reinforcing bars within a section were averaged. The strains were measured while loading the specimens, using the strains of the unloaded specimens as a reference. The effect of restrained shrinkage was neither measured nor estimated due to the complexity of the phenomenon with non-homogeneous reinforcement and deformations in this region. The implications of neglecting restrained shrinkage on the estimation of bond shear stresses will be discussed in Sections 3.2 and 4.2. As the cracks rarely formed exactly at the location of the strain gauges, the measured strains ($\varepsilon_{s,exp}$) might not correspond to the maximum strain of the reinforcement at the crack (ε_s). The distance between the strain gauge and the main crack at the re-entrant corner (Δ) was measured in each test, which allowed to

Table 2
Mechanical properties of the used reinforcing steel.

		Reinforcing bar diameter [mm]						
		6	8	10	12	16	20	25
Specimens DEB-:	f_y [MPa]	605.4	619.0	566.5	585.0	-	536.2	-
1.1, 1.2, 1.3, 1.4, 1.5, 2.1	f_u [MPa]	713.1	708.9	655.0	672.5	-	655.5	-
Specimens DEB-:	f_y [MPa]	547.3	532.3	544.2	546.1	549.6	-	569.9
1.6, 1.7, 1.8, 1.9, 2.2, 2.3	f_u [MPa]	680.1	672.1	654.3	658.5	672.8	-	695.9
Specimens DEB-:	f_y [MPa]	558.6	554.1	548.4	551.7	543.9	-	539.9
2.4, 2.5, 2.6	f_u [MPa]	718.2	673.5	656.2	640.1	638.3	-	650.9

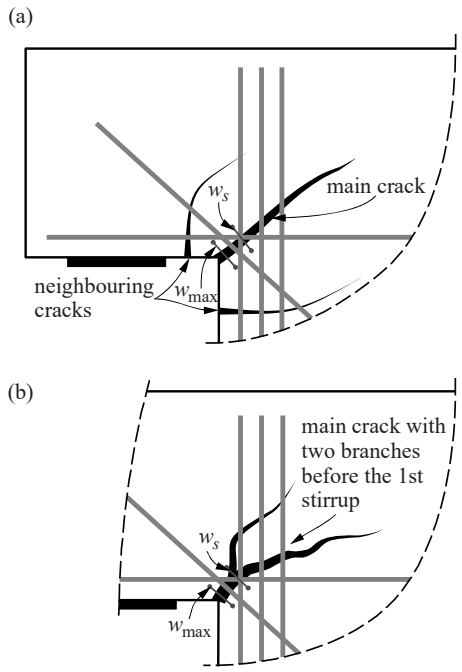

Fig. 4. Conceptual crack behaviour with definition of neighbouring and branching cracks.

estimate the strains of the reinforcement at the crack in the serviceability range (reinforcement stayed elastic) by assuming a constant bond distribution:

$$\varepsilon_s = \varepsilon_{s,exp} + \frac{\Delta}{\varnothing}\frac{4\tau_{b0}}{E_s} \tag{1}$$

where $\varnothing$ is the diameter of the reinforcing bar, E_s the Young's modulus of the reinforcement and τ_{b0} the bond shear stress in the elastic range that was assumed to be $\tau_{b0} = 2f_{ctm}$ according to the Tension Chord Model (TCM) [25]. f_{ctm} is the mean tensile strength which was estimated based on the measured cylindrical compressive strength as follows (according to Eurocode 2 [2]):

$$f_{ctm} = 0.3f_c^{2/3} \tag{2}$$

The 2D-DIC post-processing comprised measurements of the maximum crack widths (in the re-entrant corner) and full-field measurements in selected beams to evaluate the development and distribution of all cracks forming in the vicinity of the re-entrant corner. The maximum crack width was measured using a tracking approach of individual points, developed at the Universitat Politècnica de València, implementing suitable calibration approaches [26,27]. The displacement and the strain fields were computed using the commercial software VIC-2D from Correlated Solutions Inc. [28]. Following the recommendations of Mata-Falcón et al. [29], the following settings were taken as correlation parameters: subset size = 29 px, step size = 7 px and strain filter size = 7. Crack widths at different locations were extracted by manually placing virtual extensometers perpendicular to the crack direction identified by the principal strain results from the DIC analysis.

For three selected tests (DEB-1.6 (T1), DEB-1.7 (T2) and DEB-2.2 (T2)), the full-field DIC results were further post-processed using the automatic crack detection and measurement tool (ACDM) [30,31]. For the crack detection method, edge detection with a low and high strain threshold at 1 and 15‰ was chosen. For visualisation purposes, crack line smoothing with a filter span of 3 and the smoothing method 'moving' was applied. Further details will be described in Section 3.2.

3. Results and discussion

3.1. Overview

This section describes the main results of the experimental campaign in terms of its serviceability behaviour (Serviceability Limit State (SLS)). The service load considered during design is highly dependent on the type of actions on the structure, but it usually ranges between 0.3 and 0.6 of the Ultimate Limit State (ULS) design load.

The failure of the beam generally occurred in the tested support. However, in DEB-1.1 (T2), DEB-1.5 (T2), DEB-2.3 (T2) and DEB-2.6 (T2), the first test on the beam specimen pre-damaged the opposite discontinuity region. The last two tests were discarded entirely for this analysis. In contrast, the first two were included, as the pre-damage was found to influence only the ultimate behaviour, which is of secondary interest in this work. In all cases, after significant yielding of the dapped-end reinforcement, failure of concrete occurred with or without spalling of the top cover of the beam. Further details on the ultimate load behaviour can be found elsewhere [7].

At the beginning of the experiment, a large crack formed at the re-entrant corner of all tested beams and propagated towards the dapped-end reinforcement, hereafter referred to as the main crack. The opening of the main crack next to the re-entrant is denoted by w_{max}, see Fig. 4. In some tests, the main crack split into branches (see Fig. 4b), while neighbouring cracks formed typically much later than the main crack. Further details of the crack behaviour are given in Section 3.2, while the influence of the different reinforcement configurations on the crack width will be discussed in Section 3.4.

Table 3 summarises the experimental results, including the ultimate load V_u, the maximum crack widths at the re-entrant corner w_{max} for different load levels and the selection criteria for the tests used in Section 4.2 to estimate the bond shear stress. These results are discussed in the following sections. Firstly, the focus lies on the crack formation and kinematic behaviour in Section 3.2. Secondly, the distribution of the load-bearing capacity between the hanger and the diagonal reinforcement is examined in Section 3.3, followed by a discussion of the maximum crack width in Section 3.4.

3.2. Crack formation and kinematics

This section describes the crack formation and kinematic behaviour, starting with an in-depth analysis of three tests. Furthermore, strain results of the dapped-end reinforcement of two tests are also presented to gain insights into the bond behaviour.

The detailed crack behaviour at the re-entrant corner of three selected tests (DEB-1.6 (T1), DEB-1.7 (T2) and DEB-2.2 (T2)) is investigated and shown in Fig. 5 at different relative load levels of the ultimate load (0.2, 0.4 and 0.6). The behaviour is obtained by post-processing the DIC full-field strain results using ACDM [30,31]. The tests were selected to include specimens with and without diagonal reinforcement and to cover the different crack behaviours observed during the test series.

For DEB-1.7 (T2), a main crack formed first and then split into two branches after crossing the second stirrup of the vertical dapped-end reinforcement. At the load $0.6V_u$ = 113.3 kN, a second crack had developed on the right side of the main crack. In comparison with the other two tests, the maximum crack width for DEB-1.7 (T2) was larger at similar loads. For DEB-2.2 (T2), the main crack exhibited a complex behaviour, merging with a near crack and containing several branches. In addition, multiple secondary cracks had formed at a load of $0.6V_u$ = 197.9 kN. In DEB-1.6 (T1), the main crack had already divided into two branches before crossing the first stirrup. With increasing load, several neighbouring cracks appeared. For all three selected tests and all load levels, the main crack starting at the re-entrant corner had the largest crack width compared with the secondary cracks.

From these observations, the crack behaviour of all tests was

Table 3
Overview of the experimental results, including ultimate load, cracks at different load levels ($V = 0.2$, 0.4 and $0.6V_u$), strains at $0.4V/V_u$, angle of the crack and how and which tests were selected for the estimation of the bond shear stress (* indicates pre-damage from the first test that might have affected the failure behaviour of the second test).

		Ultimate load	Maximum crack width w_{max} [mm]			Reinf. strains $\varepsilon_{s,H}$[‰]	$\varepsilon_{s,V}$ [‰]	Loads at w_{max} V [kN]				Crack angle	Only one main crack	No secondary cracks after $w_{max} = 0.35$ mm	Selected for bond estimation (Section 4.2)
Specimen	**Layout**	V_u [kN]	$0.2V_u$	$0.4V_u$	$0.6V_u$	$0.4V_u$	$0.4V_u$	0.1 mm	0.2 mm	0.4 mm	0.6 mm	θ_c [°]			
DEB-1.1 (T1)	O.1	193.6	0.08	0.54	1.12	1.77	1.95	42.0	53.8	69.5	81.7	51	Yes	Yes	No
DEB-1.1 (T2)	O.1	209.2 *	0.10	0.57	1.16	2.11	2.19	43.8	53.7	69.8	86.3	40	Yes	Yes	No
DEB-1.2 (T1)	O.2	145.8	0.00	0.32	0.68	1.78	1.71	46.8	48.7	66.3	82.2	36	Yes	Yes	Yes
DEB-1.2 (T2)	O.2	132.7	0.06	0.40	0.71	2.18	1.44	34.6	37.4	53.4	71.9	33	Yes	No	No
DEB-1.3 (T1)	O.3	121.1	0.01	0.17	0.63	1.05	1.23	46.5	50.0	59.7	71.1	45	No	-	No
DEB-1.3 (T2)	O.3	133.0	0.04	0.23	0.80	1.06	1.15	41.4	50.7	62.2	68.7	45	No	-	No
DEB-1.4 (T1)	O.1	183.0	0.03	0.36	0.62	2.05	1.84	39.2	52.5	77.9	105.4	45	No	-	No
DEB-1.4 (T2)	O.1	170.4	0.05	0.46	1.06	2.11	2.54	41.6	48.6	63.2	78.4	40	Yes	Yes	Yes
DEB-1.5 (T1)	O.2	125.3	0.01	0.42	0.76	2.31	2.38	35.2	38.2	48.9	63.6	45	No	-	No
DEB-1.5 (T2)	O.2	177.3 *	0.16	0.64	1.52	2.94	2.12	34.2	37.6	52.6	68.8	31	Yes	Yes	Yes
DEB-1.6 (T1)	O.1	309.2	0.16	0.47	0.78	1.46	1.99	47.8	70.5	106.2	152.9	45	No	Yes	No
DEB-1.6 (T2)	O.1	250.9	0.16	0.61	0.96	1.14	1.80	29.9	56.7	80.0	99.6	52	No	No	No
DEB-1.7 (T1)	O.2	194.4	0.08	0.36	0.71	1.21	1.85	41.6	55.4	82.4	99.1	36	No	Yes	No
DEB-1.7 (T2)	O.2	188.8	0.11	0.46	0.99	1.44	1.52	36.1	46.6	70.1	87.3	37	Yes	Yes	Yes
DEB-1.8 (T1)	O.1	195.3	0.12	0.44	0.74	1.48	2.16	34.6	49.4	74.0	94.4	62	Yes	No	No
DEB-1.8 (T2)	O.1	199.1	0.08	0.40	0.82	1.74	1.90	44.0	60.1	79.5	100.2	45	Yes	No	No
DEB-1.9 (T1)	O.2	141.7	0.04	0.30	0.59	1.25	1.51	36.4	46.8	67.5	86.5	48	Yes	No	No
DEB-1.9 (T2)	O.2	145.5	0.05	0.32	0.65	1.42	1.17	35.0	43.4	66.2	82.5	36	Yes	Yes	Yes
DEB-2.1 (T1)	D.1	194.9	0.02	0.27	0.81	1.14	1.33	55.9	69.5	86.8	100.4	50	Yes	Yes	Yes
DEB-2.1 (T2)	D.1	199.6	0.09	0.50	1.03	1.21	1.37	40.8	49.6	71.6	87.7	36	Yes	Yes	Yes
DEB-2.2 (T1)	D.1	321.8	0.08	0.42	0.63	1.25	1.40	72.0	94.4	126.4	180.6	44	Yes	Yes	Yes
DEB-2.2 (T2)	D.1	329.8	0.10	0.39	0.63	1.08	1.43	65.3	91.8	134.1	187.3	41	Yes	Yes	Yes
DEB-2.3 (T1)	D.1	240.5	0.06	0.31	0.60	1.44	1.12	55.7	73.8	109.8	144.0	39	No	No	No
DEB-2.4 (T1)	D.2	311.9	0.10	0.32	0.54	1.68	1.04	61.1	88.8	147.2	207.3	34	Yes	No	No
DEB-2.4 (T2)	D.2	309.4	0.12	0.46	0.63	1.45	1.56	55.1	82.0	115.1	164.0	38	Yes	Yes	Yes
DEB-2.5 (T1)	D.3	265.1	0.10	0.29	0.48	1.82	-	53.7	78.4	129.7	196.7	44	Yes	No	No
DEB-2.5 (T2)	D.3	294.9	0.08	0.26	0.40	2.33	1.45	64.6	97.0	175.8	245.4	45	No	-	No
DEB-2.6 (T1)	D.4.1	328.1	0.10	0.38	0.67	0.97	2.10	66.9	93.7	136.3	178.6	45	Yes	No	No

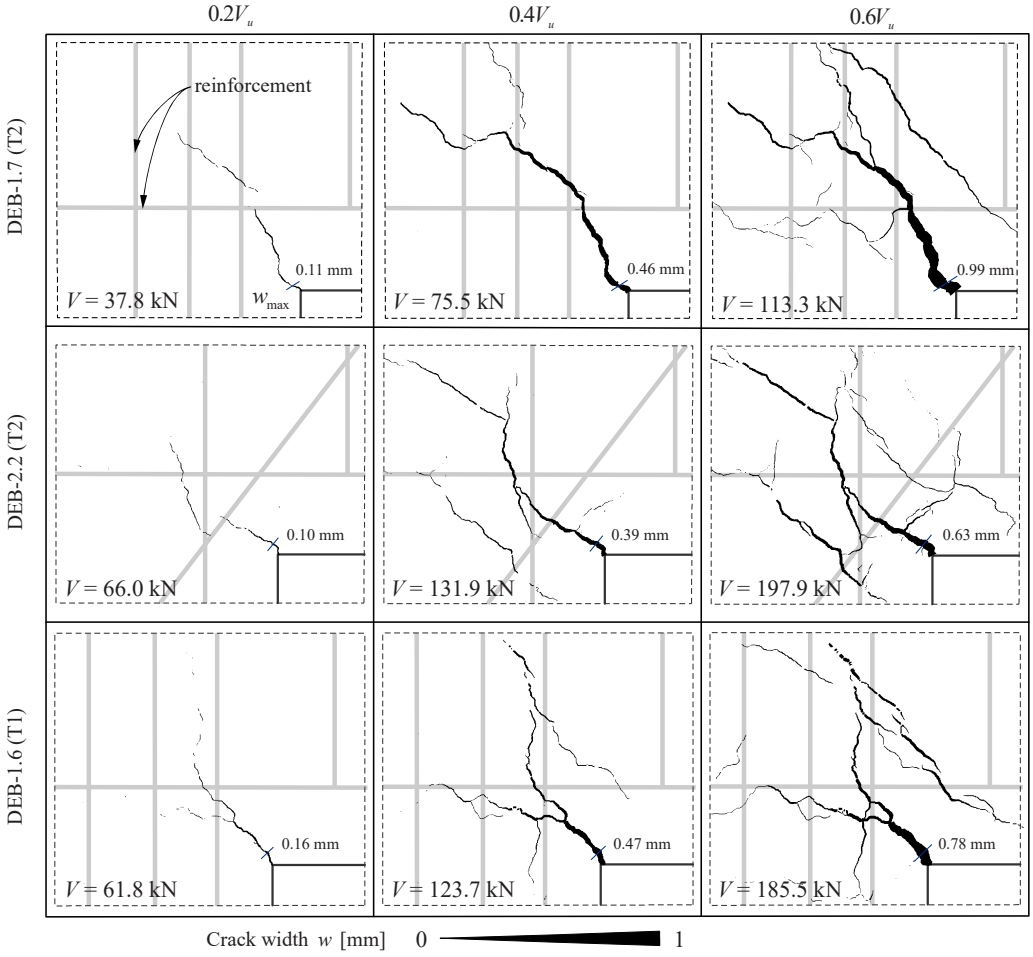

Fig 5. Crack patterns for three exemplary tests across three serviceability stages near the re-entrant corner, with the line thickness corresponding to the crack width.

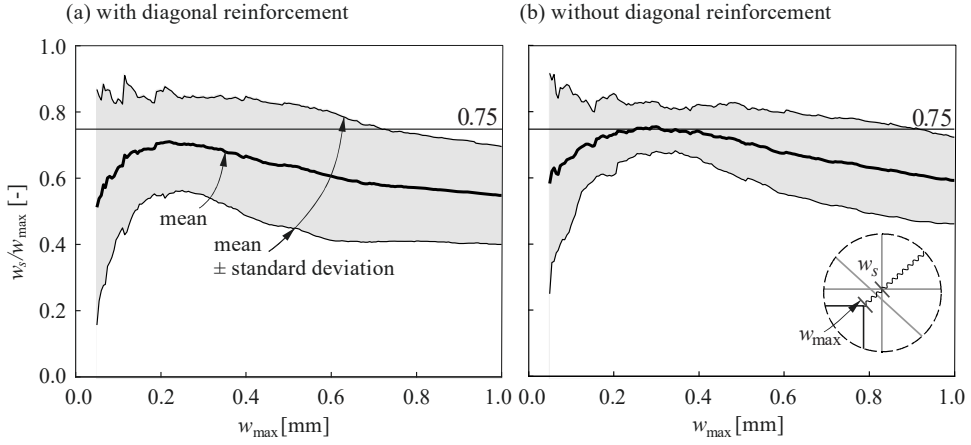

Fig. 6. Ratio of crack width at the reinforcement location over maximum crack width.

categorised based on the branching of the main crack and when the secondary cracks had formed (see Table 3). The main crack was classified as a single crack if it did not split into two branches before reaching the first stirrup of the vertical dapped-end reinforcement during serviceability (up to $w_{max} = 0.4$ mm). The classification was achieved by visual inspection of the crack patterns. From the tests shown in Fig. 5, the main crack of DEB-1.6 (T1) was classified as a branching crack, while for DEB-1.7 (T2) and DEB-2.2 (T2), a single crack is assumed given the branching of the main crack occurred at a later stage. In addition to the main crack width, the crack widths of the neighbouring cracks at and in the direction of the reinforcing bars were also extracted from the DIC strain results by manually placing virtual extensometers. This analysis was conducted for all tests except for DEB-1.3 (T1), DEB-1.3 (T2), DEB-1.4 (T1), DEB-1.5 (T1) and DEB-2.5 (T2), for which multiple main cracks were observed during visual inspection. The tests were then categorised as having significant secondary cracks if the secondary cracks that had formed, before the main crack reached a crack width of $w_{max} = 0.35$ mm. A crack width threshold of 0.05 mm was used to detect the

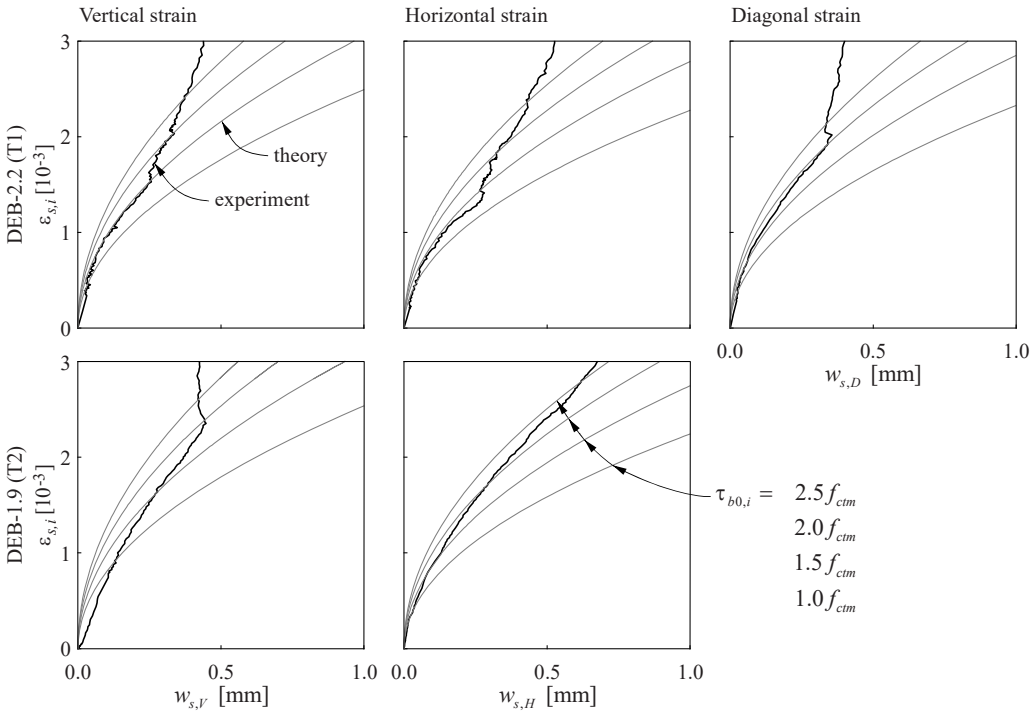

Fig. 7. Crack behaviour of DEB-2.2 (T1) and DEB-1.9 (T2), where the reinforcement strains $\varepsilon_{s,i}$ are plotted against the projection of the crack width in the corresponding reinforcement direction $w_{s,i}$ (the theoretical relationship for different bond strengths is included in grey for comparison).

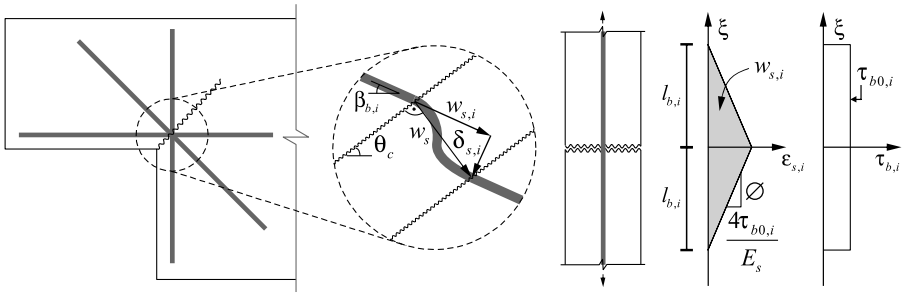

Fig. 8. Analytical model to estimate the crack width of the re-entrant corner at the intersection with the reinforcement based on the reinforcement strains at the crack.

secondary cracks.

The conducted local analysis allowed by the application of novel automated crack width measurements reveals that the kinematics of the cracks at the re-entrant corner are complex and vary considerably between the tests. The width of the main crack when crossing the reinforcement is highly dependent on the actual crack pattern of the beam and is subjected to high scatter. In the frequent case of branching cracks, it is unclear if the local crack width measurement is representative. While for durability aspects the local width of each crack branch crossing the reinforcement is decisive, the superposed width of the crack branches could be more representative to quantify the activation of the reinforcement. To avoid this uncertainty, the width of the main crack is measured for comparison purposes in all beams close to the re-entrant corner, where no branching was happening (see definition of $w_{\max}$ in Fig. 4). However, to correlate the crack width with the measured reinforcement strains, it is crucial to estimate the effective width that the main crack would have had when crossing the orthogonal reinforcement (see definition of w_s in Fig. 4) if no branching had occurred. To estimate w_s based on the measured crack width $w_{\max}$, their relative values were analysed in Fig. 6 for the tests with full-field DIC analyses. It can be seen that within the crack formation, the ratio increased and began to drop due to the formation of secondary cracks at around $w_{\max} = 0.25$ mm and $w_{\max} = 0.30$ mm for beams with and without diagonal reinforcement, respectively. The variance of the crack width ratio is greater for beams with diagonal reinforcement than for those without. For the beams in this experimental campaign, a rule of thumb for estimating the width of the main crack at the reinforcement is $w_s = 0.75 w_{\max}$ when neither branching nor secondary cracks are present or of interest. However, this ratio is highly dependent on the configuration of the reinforcement, e.g. reinforcement ratio, and the geometry of the dapped end, which ultimately leads to different depths of the compression zone.

Tests DEB-1.9 (T2) and DEB-2.2 (T1) were further analysed to understand the crack and bond behaviour of the dapped-end reinforcement more in detail. The measured strains of each dapped-end reinforcement ($\varepsilon_{s,i}$) are represented in Fig. 7 (black curves) against the projection of the crack width at the reinforcement (w_s) in the corresponding reinforcement direction ($w_{s,i}$). Their correlation provides an estimate of the reinforcement engagement, which is directly dependent on the bond between the reinforcing bar and the surrounding concrete. When assuming constant bond stress along the reinforcing bar and the isolated main crack (affected neither by branching nor by secondary cracks), the projection of the crack width in the direction of the reinforcement ($w_{s,i}$) is related to the reinforcement strains at the crack ($\varepsilon_{s,i}$) as follows (see also Fig. 8):

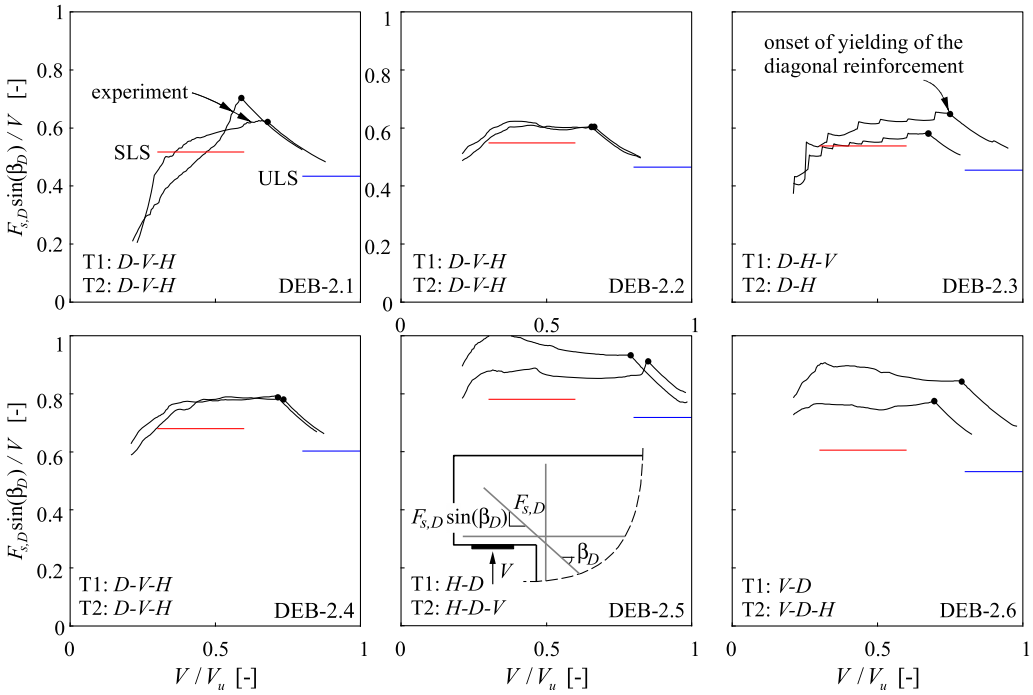

Fig. 9. Load fraction of the support load V carried by the diagonal reinforcement.

$$w_{s,i} = \frac{\varnothing_i}{4}\cdot\frac{\varepsilon_{s,i}^2 E_s}{\tau_{b0,i}} \quad \text{for } i = H, V, D \tag{3}$$

Eq. (3) implies a parabolic relationship between the crack width and the reinforcement strains. The highest uncertainty in this relationship is the bond strength value to be considered. While for elements subjected to bending or uniaxial tension there is a consensus that a value of $\tau_{b0} = 2f_{ctm}$ as proposed by the TCM [25] is reasonable, very different bond values for the main reinforcement in dapped-end beams have been suggested [12,21]. Differences in the bond behaviour close to the re-entrant corner could be due to the distinct concentration of restrained shrinkage strains and reinforcement in several directions. Eq. (2) is plotted in Fig. 7 for different levels of the bond shear stress τ_{b0} (grey curves) to gain more information about the bond behaviour. The experimental results in Fig. 7 should be interpreted with care because the measured strains do not account for the initial compressive strains in the reinforcement due to restrained shrinkage (see Section 2.2), which means that the actual $\varepsilon_{s,i}$-w_s curves considering the actual strains would be slightly moved down. For DEB-2.2 (T1), the strain measurements coincided with a constant bond shear stress of approximately $1.5f_{ctm}$ for the orthogonal reinforcing bars up to 0.3 mm of the corresponding crack width. Whereas for the diagonal reinforcement it was proportional to a bond shear stress of $2.0f_{ctm}$ until $w_{s,D} = 0.4$ mm. For larger crack widths, the main crack is no longer isolated, and any bond conclusion drawn from Eq. (3) is no longer valid. The bond strength in DEB-2.2 (T1) is in a similar range as recommended by the TCM. In DEB-1.9 (T2), the experimental results do not follow a clear parabolic relationship and no clear conclusions about a constant bond strength can be stated. Further analyses will be presented in Section 4.2 to define the specific bond strength to be considered in the proposed model.

3.3. Distribution of the load-bearing capacity in beams with diagonal reinforcement

This section describes the load-bearing distribution between the hanger and the diagonal reinforcement for beams with diagonal reinforcing bars. The forces carried by the diagonal reinforcement ($F_{s,D}$) were determined from the experimental strain measurements at the crack forming at the re-entrant corner by applying a simplified bilinear stress-strain relationship for the reinforcement steel with Young's modulus of 200 GPa, ultimate strain of 8 % and with the mechanical properties given in Table 2. The fraction of the load V carried by the diagonal reinforcement is shown in Fig. 9, which also shows the onset of yielding of the diagonal reinforcement with a black dot and the sequence of yielding at the bottom-left side of each plot [7]. At low load levels, these experimental results are not sufficiently reliable since (i) the concrete itself might resist part of the load V (e.g. through aggregate interlock or residual tensile strength) and (ii) the strain gauges might not be directly located at the crack, providing inaccurate estimations of the corresponding steel force. Therefore, the measurements up to a load level of 20% are excluded and not plotted in Fig. 9. The proportion of the load carried by the diagonal reinforcement increased up to a load level of approximately 30%, at which it reached a plateau. This plateau indicates that the steel force in the diagonal reinforcing bar increased directly proportionally to the load. Hence, this plateau represents the load distribution between the diagonal and hanger reinforcement. The plateaus of the tests with the reinforcement layout D.1 (DEB-2.1, DEB-2.2 and DEB-2.3) all stagnate around a ratio of 0.57, while they increase to values between 0.76 and 0.89 in the other tests, or even 0.98 in the case of test DEB-2.5 (T2). Once the diagonal reinforcement starts to yield (indicated by black dots), this fraction begins to decrease at approximately 75% of the ultimate load level. In that case, the elastic hanger reinforcement had to resist most of the remaining load increments, since the additional load taken by the diagonal reinforcement during hardening is minimal. Between the load levels of 80% and 90%, the strain gauges were damaged during the test and no strain measurements could be obtained after this point. The strut-and-tie model for ultimate load by Mata-Falcón et al. [7] estimates the load carried by the diagonal reinforcement (blue line in Fig. 9, 1-X_{ULS} in Table 4, where X_i, with i = *ULS, SLS*, refers to the proportion of the load V carried by the vertical reinforcement). However, during serviceability, the diagonal reinforcement was not yet yielding and the results show that the fraction of the load carried by the diagonal reinforcement was significantly larger than at failure.

Table 4
Overview of the load factors that characterise the strut-and-tie model, comparing the experimental values at serviceability with the model predictions at ULS and SLS (* marks missing strain measurements due to damaged strain gauge), and the mean and coefficient of variation (CV).

	Experiment at SLS			Model at ULS			Model at SLS			Experiment/Model at SLS		
Specimen	$\alpha_{V,exp}$	$\alpha_{H,exp}$	X_{exp}	$\alpha_{V,ULS}$	$\alpha_{H,ULS}$	X_{ULS}	$\alpha_{V,SLS}= \kappa_V \alpha_{V,ULS}$	$\alpha_{H,SLS}= \kappa_H \alpha_{H,ULS}$	X_{SLS}	$\alpha_{V,exp}/\ \alpha_{V,SLS}$	$\alpha_{H,exp}/\ \alpha_{H,SLS}$	X_{exp}/X_{SLS}
DEB-1.1 (T1)	1.32	1.76	1.00	0.86	1.14	1.00	1.20	1.59	1.00	1.10	1.10	1.00
DEB-1.1 (T2)	1.24	1.92	1.00	0.86	1.14	1.00	1.20	1.59	1.00	1.03	1.21	1.00
DEB-1.2 (T1)	1.48	1.28	1.00	1.17	1.07	1.00	1.64	1.50	1.00	0.90	0.85	1.00
DEB-1.2 (T2)	1.28	1.85	1.00	1.17	1.07	1.00	1.64	1.50	1.00	0.79	1.24	1.00
DEB-1.3 (T1)	0.50	1.61	1.00	0.50	1.14	1.00	0.70	1.60	1.00	0.71	1.01	1.00
DEB-1.3 (T2)	0.47	1.57	1.00	0.50	1.14	1.00	0.70	1.60	1.00	0.67	0.98	1.00
DEB-1.4 (T1)	1.31	2.15	1.00	0.95	1.30	1.00	1.33	1.73	1.00	0.99	1.24	1.00
DEB-1.4 (T2)	1.84	2.01	1.00	0.95	1.30	1.00	1.33	1.73	1.00	1.38	1.16	1.00
DEB-1.5 (T1)	2.21	1.87	1.00	1.44	1.23	1.00	2.02	1.72	1.00	1.10	1.09	1.00
DEB-1.5 (T2)	1.24	2.01	1.00	1.44	1.23	1.00	2.02	1.72	1.00	0.61	1.17	1.00
DEB-1.6 (T1)	1.71	1.96	1.00	1.05	1.58	1.00	1.47	1.73	1.00	1.16	1.13	1.00
DEB-1.6 (T2)	1.95	1.82	1.00	1.05	1.58	1.00	1.47	1.73	1.00	1.32	1.05	1.00
DEB-1.7 (T1)	2.59	1.43	1.00	1.63	1.37	1.00	2.29	1.73	1.00	1.13	0.82	1.00
DEB-1.7 (T2)	2.14	1.72	1.00	1.63	1.37	1.00	2.29	1.73	1.00	0.94	0.99	1.00
DEB-1.8 (T1)	2.03	2.16	1.00	0.96	1.42	1.00	1.34	1.73	1.00	1.51	1.25	1.00
DEB-1.8 (T2)	1.73	2.46	1.00	0.96	1.42	1.00	1.34	1.73	1.00	1.29	1.42	1.00
DEB-1.9 (T1)	1.95	1.47	1.00	1.42	1.30	1.00	1.98	1.73	1.00	0.98	0.85	1.00
DEB-1.9 (T2)	1.48	1.64	1.00	1.42	1.30	1.00	1.98	1.73	1.00	0.75	0.95	1.00
DEB-2.1 (T1)	1.15	1.52	0.49	0.81	1.08	0.57	1.14	1.51	0.48	1.01	1.00	1.01
DEB-2.1 (T2)	1.23	1.76	0.44	0.81	1.08	0.57	1.14	1.51	0.48	1.08	1.17	0.92
DEB-2.2 (T1)	1.68	2.17	0.40	0.92	1.21	0.54	1.29	1.70	0.45	1.30	1.28	0.89
DEB-2.2 (T2)	1.73	1.82	0.39	0.92	1.21	0.54	1.29	1.70	0.45	1.34	1.07	0.87
DEB-2.3 (T1)	1.18	2.21	0.45	0.84	1.15	0.55	1.17	1.60	0.46	1.01	1.38	0.98
DEB-2.4 (T1)	1.68	3.58	0.23	0.90	1.15	0.40	1.25	1.61	0.32	1.34	2.22	0.72
DEB-2.4 (T2)	2.35	3.04	0.24	0.90	1.15	0.40	1.25	1.61	0.32	1.87	1.89	0.75
DEB-2.5 (T1)	*	4.11	0.13	0.65	1.10	0.28	0.91	1.54	0.22	*	2.68	0.58
DEB-2.5 (T2)	4.46	9.58	0.02	0.65	1.10	0.28	0.91	1.54	0.22	4.90	6.24	0.10
DEB-2.6 (T1)	2.91	10.69	0.11	0.33	1.39	0.47	0.47	1.73	0.39	6.22	6.17	0.29
							Mean of DEB-1.X			1.02	1.08	1.00
							CV of DEB-1.X			0.25	0.15	1.00
							Mean of DEB-2.X (excluding DEB-2.5 and DEB-2.6)			1.28	1.43	0.88
							CV of DEB-2.X (excluding DEB-2.5 and DEB-2.6)			0.30	0.46	0.11
							Mean of all tests (excluding DEB-2.5 and DEB-2.6)			1.09	1.18	0.97
							CV of all tests (excluding DEB-2.5 and DEB-2.6)			0.26	0.26	0.08

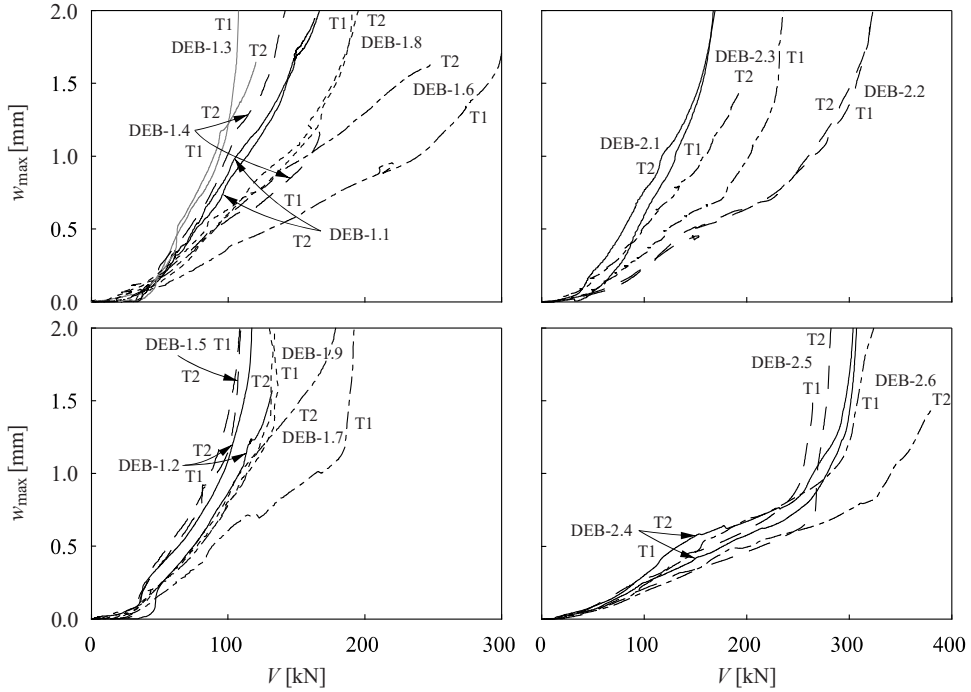

Fig. 10. Results of the maximum crack widths at the re-entrant corner.

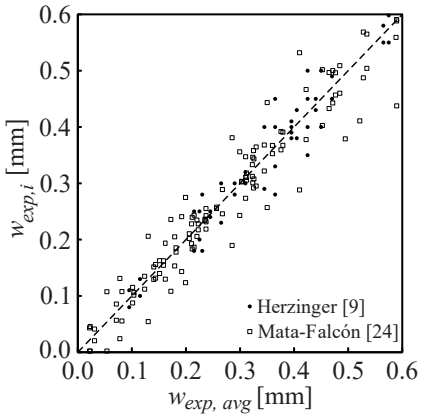

Fig. 11. Scatter of the crack width measurements at identical load levels of twin tests (0.25, 0.35, and 0.45V_u).

3.4. Maximum crack width

As mentioned in Section 3.2, the maximum crack width is considered to be a consistent parameter between the different tests and used as the main comparative measure of the crack development. The load-crack width relationship for all the tests, including DEB-2.3 (T2) and DEB-2.6 (T2), is presented in Fig. 10. The top left subfigure includes Layouts O.1 (in black) and O.3 (in grey), the bottom left one only Layout O.2, the top right one Layout D.1 and lastly, the bottom right one the remaining layouts with diagonal reinforcement: D.2, D.3 and D.4.1.

DEB-1.4, DEB-1.6, DEB-1.7, DEB-2.3 and DEB-2.6 exhibited more scatter than the other beam specimens. The variance of the last two specimens can be partly explained by the pre-damage of the second dapped end, already described in Section 3.1. For all the first tests of these beams with orthogonal reinforcement, the main crack split before reaching the first stirrup. Furthermore, the first test demonstrated a stiffer behaviour, indicating possible pre-damage on the second tested support. The scatter is further illustrated in Fig. 11, which also includes experiments from Herzinger [9].

Increasing the reinforcement content of the same layout resulted in a stiffer behaviour of the tests until yielding of the reinforcement and a higher load-bearing capacity. Distributing the vertical dapped-end reinforcement led to a more uncertain or less stiff behaviour when comparing DEB-1.4, respectively DEB-1.5, with DEB-1.1, respectively DEB-1.2. Beam DEB-1.3 with reinforcement layout O.3, in which 60% less hanger reinforcement was used, had a much lower load-bearing capacity (reduction of 37%) compared to its reference specimen DEB-1.1 with Layout O.1. Its crack widths also measured increasingly higher values with growing support loads (19% and 43% for $V = 50$ and 100 kN). Comparing the beams with and without diagonal reinforcement, shows that the additional diagonal reinforcing bars helped to reduce the maximum crack width.

To compare different reinforcement layouts and contents with each other, Fig. 12 shows the average load-crack width behaviour between the twin tests as a function of the load level relevant for serviceability verification (up to $0.6V/V_u$). Comparing reinforcement layout O.2, where the horizontal reinforcement amount was 40% lower, with the reference layout O.1, the overall behaviour was softer and had a lower variance between the tests, except for the second tests of Beams DEB-1.4, DEB-1.6 and DEB-1.7. The experimental ultimate load was approximately 30% lower. Similarly, the crack widths of Layout O.2 were larger than those of the reference layout for a given load: E.g. the increase in crack width varied at a load of $V = 50$ kN or 100 kN, between 41% and 78% or 15% and 45%, respectively, depending on the reinforcement ratio (Fig. 10).

For the beams with diagonal reinforcement, the load-crack width behaviour of the under-reinforced layouts D.2 and D.3 did not differ much from their reference layout D.1. Even compared to their orthogonal counterparts, the reduction in ultimate load-bearing capacity was much less pronounced (5% and 14%). Up to a load level of about 30%, the average crack width was consistent between the different layouts. Considering the same loads, $V = 50$, 100 and 150 kN, the crack widths were of similar magnitudes compared to Layout D.1: varying between -3% and 29% for D.2 and -21% and 18% for D.3 (Fig. 10). However, Layout D.3 exhibited the stiffest behaviour, followed by Layouts D.2, D.4.1 and finally D.1.

4. Strut-and-tie model for serviceability crack width predictions

The proposed model for serviceability is based on a strut-and-tie model developed by the authors for ultimate loads [7]. The first section of this chapter summarises the relevant parts of the existing model and presents the assumptions and modifications of the strut-and-tie model for service loads. Section 4.2 studies the value of the bond shear stresses that are appropriate to consider in the model, while Section 4.3 describes the differences between the behaviour under service and ultimate loads.

4.1. Model description

In this paragraph, the existing strut-and-tie model for ultimate loads is described conceptually [7]. The model considers the concrete above the top nodal area of the vertical reinforcement. The upper cover is often neglected due to the possibility of concrete spalling failure. However, this can lead to overly conservative assessments for existing structures

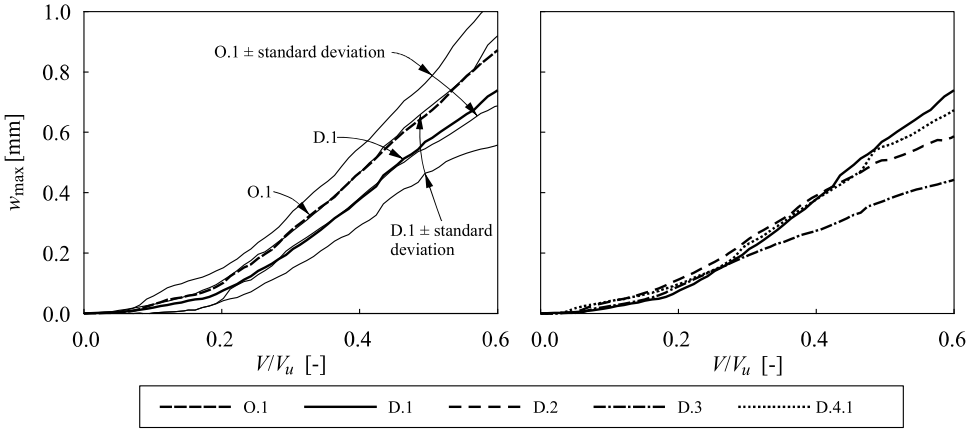

Fig. 12. Comparison of average crack widths at the re-entrant corner for several reinforcement configurations.

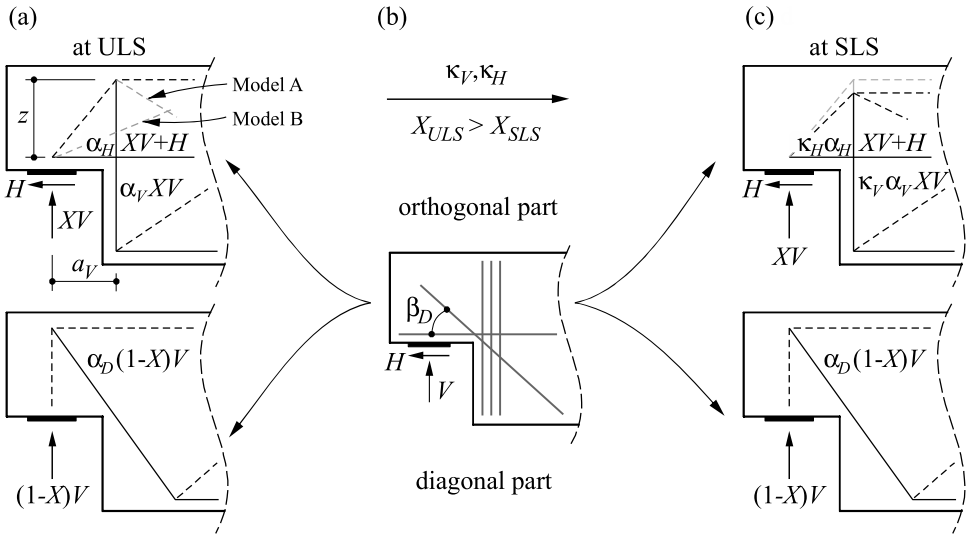

Fig. 13. Strut-and-tie model for dapped-end beams: (a) existing model for ULS [7]; (b) reinforcement configuration and serviceability correction factors; (c) proposed model for SLS.

[10,32]. The model assumes that the diagonal and horizontal reinforcement at the re-entrant corner yield. It proposes two cases depending on whether the hanger reinforcement yields as well (Model B with a second compression strut forming between the support node and the second hanger section) or not (Model A with a second compression strut developing between the top node and the horizontal reinforcement). The variants of the original model are outlined in Fig. 13a.

The existing strut-and-tie model for ultimate loads is extended for serviceability to determine strains and crack widths at the reinforcement. It splits the acting load V into one part carried by the orthogonal reinforcement (XV) and the other part by the diagonal reinforcement ($(1\text{-}X)V$). If a horizontal load force H acts, it is assumed to be directly resisted by the horizontal tie. Based on the observations of the experimental campaign, the strut-and-tie model needs to be modified so that the diagonal reinforcement resists a higher proportion of the acting load at service loads than at ultimate loads ($X_{ULS} > X_{SLS}$, see Section 3.3). This will be achieved by adapting the orthogonal resistant mechanism as shown in Fig. 13c to account for the particularities at service loads. The strut-and-tie model associated with the diagonal reinforcement remains the same for serviceability, as it is perfectly defined by equilibrium. The adaptation of the orthogonal strut-and-tie model at serviceability will be discussed in Section 4.3, after the overall methodology is presented in the following.

The steel behaviour in the serviceability range is assumed to be linear elastic, which means that the steel strains can be obtained from the division of reinforcement tie force by its cross-sectional area $A_{s,i}$ and Young's modulus E_s. The following equations relate the reinforcement strains with the respective part of the acting load:

$$\varepsilon_{s,V} = \frac{\kappa_V \alpha_V X}{A_{s,V} E_s} V, \quad \varepsilon_{s,H} = \frac{\kappa_H \alpha_H XV + H}{A_{s,H} E_s}, \quad \varepsilon_{s,D} = \frac{\alpha_D (1-X)}{A_{s,D} E_s} V \tag{4}$$

where the load factor coefficients α_i depend on the specific strut-and-tie model at ULS (i.e. geometry, reinforcement layout and material properties) and the coefficients κ_i amplify the load factor coefficients of the orthogonal reinforcement to account for the particularities at serviceability (see Section 4.3). Given that the load factor coefficients at ULS depend on the yield strength of the reinforcement, the extension to serviceability is only applicable to reinforcement of similar yield strength. This avoids that internal redistributions caused by varying yield strength can affect the elastic behaviour. The vertical load factor α_V is the ratio of the capacity of the hanger reinforcement $F_{s,V,u}$ over the difference between the predicted ultimate load $V_{u,\text{model}}$ and the vertical component of the ultimate capacity of the diagonal reinforcement $F_{s,D,u}$ to only account for the orthogonal mechanism:

$$\alpha_V = \frac{F_{s,V,u}}{V_{u,\text{model}} - F_{s,D,u}\sin(\beta_D)} \tag{5}$$

where β_D is the inclination of the diagonal reinforcement.

The horizontal load factor α_H is determined based on the inclination of the strut at failure. For serviceability calculations, it is assumed to be limited to 30°, as it is common practice in many structural design codes (e.g. SIA 262 [33]):

$$\alpha_H = \min\left(\sqrt{3}, \frac{a_v}{z}\right) \tag{6}$$

where a_v is the horizontal distance between the hanger reinforcement and the introduction of load V and z the vertical distance between the horizontal dapped-end reinforcement and the upper node of the model (see graphical definition in Fig. 13).

The diagonal mechanism is statically determinate. Hence, the diagonal load factor α_D depends only on the inclination of the diagonal reinforcement β_D:

$$\alpha_D = \frac{1}{\sin(\beta_D)} \tag{7}$$

Once the reinforcement strains have been estimated, the crack width can be calculated using the considerations already introduced in Section 3.2 (i.e. assuming a constant bond stress along the reinforcing bar and the isolated main crack, which leads to a pull-out behaviour of the reinforcement). The approach, which is only valid when the reinforcement stays in the elastic range (serviceability), is shown in Fig. 8. The projection of the crack width in the direction of the respective reinforcement ($w_{s,i}$) can then be obtained with Eq. (3). The crack width perpendicular to the reinforcement direction is indicated by $\delta_{s,i}$. Zero crack slip is assumed, which means that the crack width w_s is perpendicular to the crack opening. This is a typical consideration for the fairly straight cracks forming at the corner of dapped-end beams.

For beams with diagonal reinforcement, the crack width yielded by the diagonal reinforcement needs to be kinematically compatible with the crack widths provided by the orthogonal reinforcement:

$$w_{s,D} = w_{s,H}\cos(\beta_D) + w_{s,V}\sin(\beta_D) \tag{8}$$

This compatibility condition allows to determine the fraction X of the vertical support load V carried by the orthogonal reinforcement (for beams without diagonal reinforcement $X = 1$):

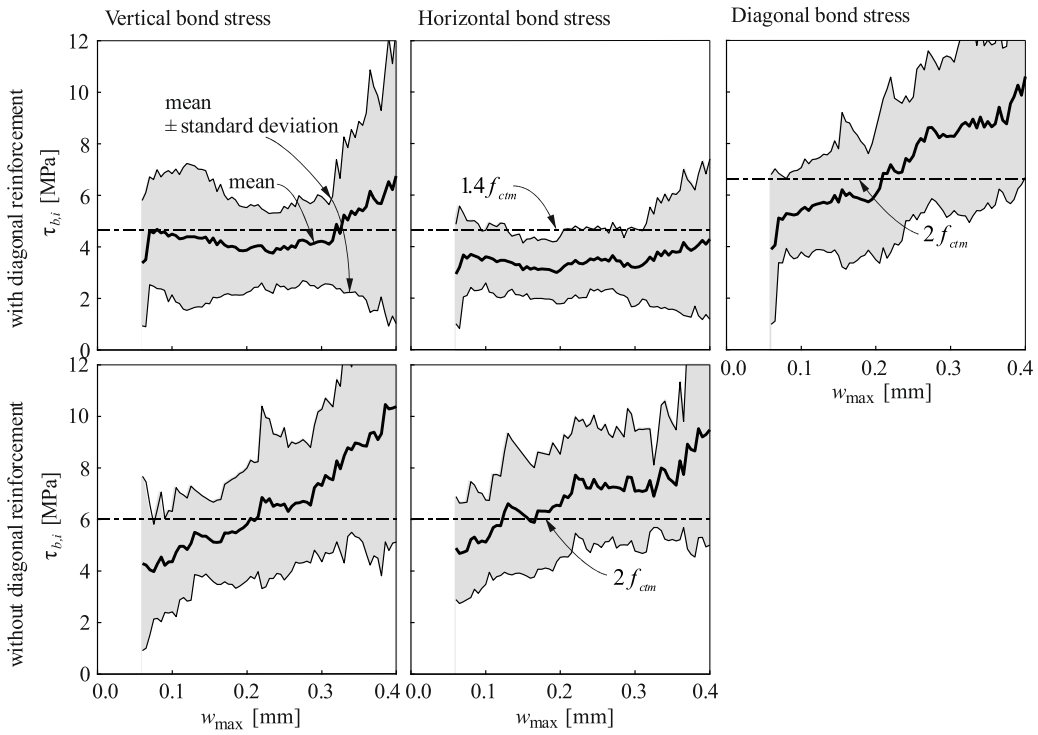

Fig. 14. Estimation of effective bond shear stresses.

$$X = \frac{1}{1 + \sqrt{\frac{\zeta_H \cos(\beta_D) + \zeta_V \sin(\beta_D)}{\zeta_D}}} \tag{9}$$

$$\text{with}: \ \zeta_D = \frac{\alpha_D^2 \varnothing_D}{A_{s,D}^2 \tau_{b0,D}} \ \text{and} \ \zeta_i = \frac{\kappa_i^2 \alpha_i^2 \varnothing_i}{A_{s,i}^2 \tau_{b0,i}} \ \text{for} \ i = H, \ V \tag{10}$$

The width of the crack when crossing the dapped-end reinforcement, which is usually the relevant crack width value for evaluating durability, can be obtained by combining its vertical and horizontal components calculated with Eq. (3):

$$w_s = \sqrt{w_{s,H}^2 + w_{s,V}^2} \tag{11}$$

The value of the crack width at the re-entrant corner (i.e. where the crack width is maximum) can be determined by correcting w_s with a factor μ_w that depends on the geometry, reinforcement layout and material properties of the dapped end:

$$w_{\max} = \frac{w_s}{\mu_w} \tag{12}$$

The factor μ_w can be estimated following the provisions given in Appendix A, which yield consistent results with the experimental observations of this study (see Section 3.2) and applies to any dapped-end configuration.

The specific values of (i) the κ_i coefficients that account for the particularities of the serviceability strut-and-tie model and (ii) the bond strength to be considered in the model will be discussed in the following sections.

4.2. Estimation of effective bond shear stresses

This section complements the experimental observations and discussion about the bond shear stresses within the serviceability range given in Section 3.2 to propose a suitable value of the average bond shear stress τ_{b0} to determine the crack behaviour of dapped-end beams. It should be noted that the herein estimated bond shear stress is not representative of the actual bond shear stresses in the region but rather an effective higher value that covers the effect of restrained shrinkage of the tests for which it was validated.

The same model as presented in Fig. 8, can also solve the inverse problem of determining the effective bond shear stresses based on known values of strains and crack widths. To remain consistent with the model proposed in Section 4.1, which does not impose strain compatibility as this would not be locally valid for the re-entrant corner of a discontinuity region, the estimation of bond shear stresses also enforces crack kinematic compatibility for the main crack. This means that the strains and bond shear stresses of different reinforcing bars must lead to the same crack. Hence, the crack widths at the reinforcement (w_s) measured with DIC are projected into the vertical, horizontal and diagonal directions using Eqs. (8) and (11) and the crack angle θ_c. The bond shear stresses can then be back-calculated with Eq. (3), the measured strains ($\varepsilon_{s,i}$) and projected crack widths ($w_{s,i}$), using the pull-out model (from TCM). The pull-out model assumes a linear elastic strain distribution for each load step, which implies that the bond shear stress along the reinforcing bar is constant. This means that no secondary cracks along the reinforcing bar should have formed. Therefore, this model is intended for serviceability and the two criteria developed in Section 3.2 need to be fulfilled for the selection of the experimental tests to be used in the estimation of the effective bond shear stresses. In this series of experiments, five tests for beams with orthogonal reinforcement only (DEB-1.2 (T1), DEB-1.4 (T2), DEB-1.5 (T2). DEB-1.7 (T2) and DEB-1.9 (T2)) and five for beams with additional diagonal reinforcement (DEB-2.1 (T1 and T2), DEB-2.2 (T1 and T2) and DEB-2.4 (T2)) have been chosen.

Fig. 14 shows the determined effective bond shear stresses of all selected tests with the mean value depicted as a thick line and the offset of one standard deviation with a shaded area in grey. For the beams with diagonal reinforcement, the orthogonal bond shear stresses show a fairly constant behaviour during serviceability, whereas the diagonal one increases linearly. Similarly, the bond shear stresses of the beams without diagonal reinforcement show a linear increase. This confirms the observations made in Section 3.2. For these three linearly increasing bond shear stresses, the effective bond shear stress has been simplified to an

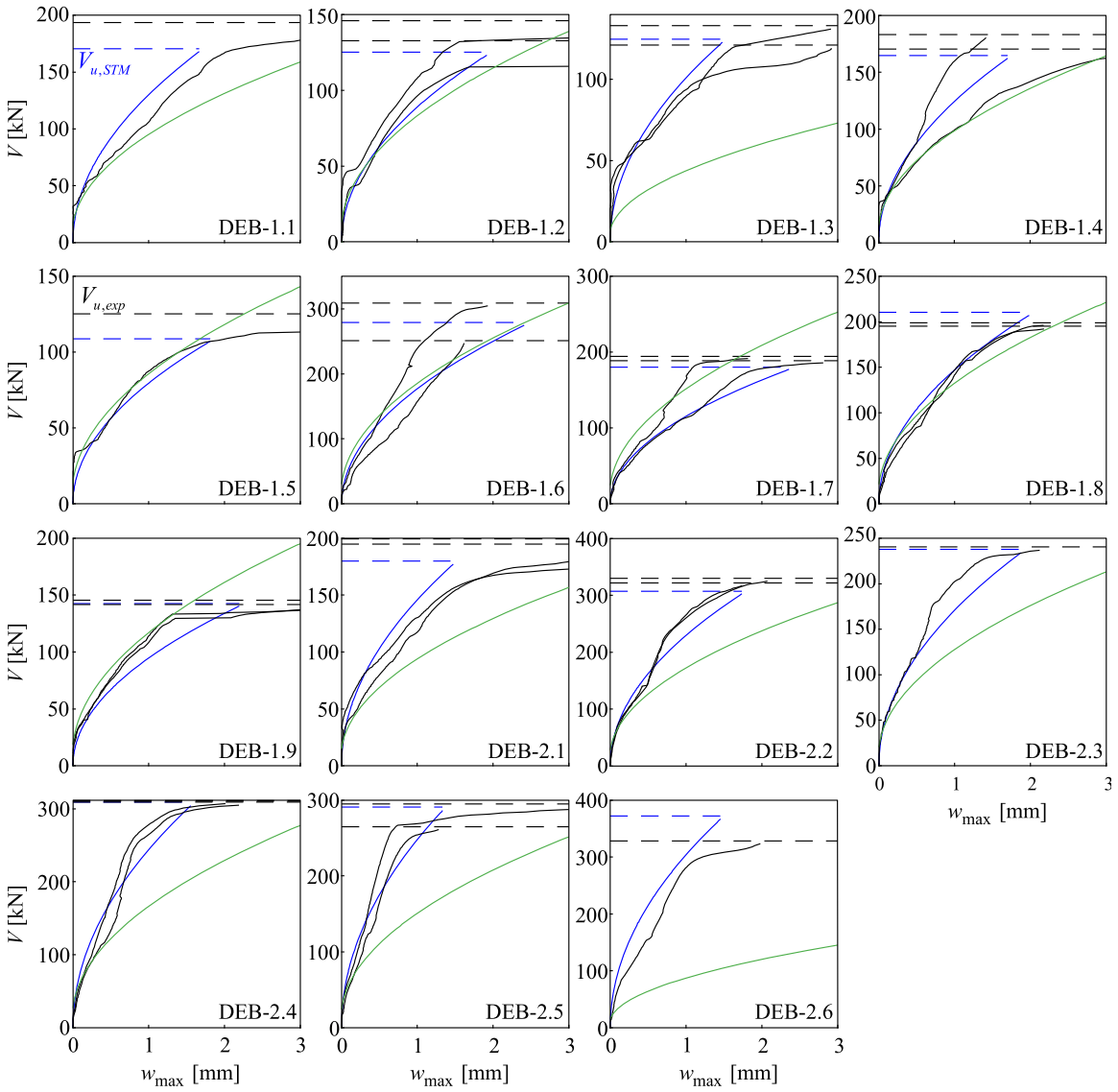

Fig. 15. Prediction of the maximum crack width (in blue) compared to the experimental values (in black) and to the predictions by Zhu et al. [11] (in green). The dashed line indicates the ultimate load from the experiments (in black) and from the ULS prediction (Mata-Falcón et al. [7], in blue).

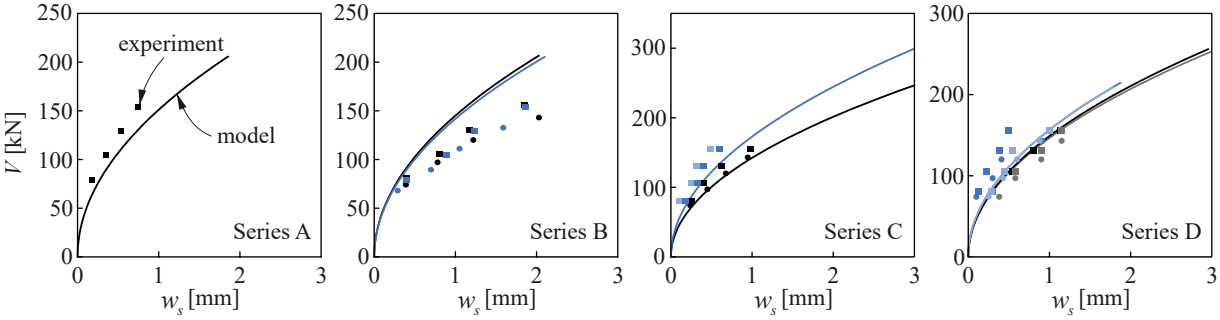

Fig. 16. Model predictions compared with experimental measurements by Herzinger [9]. ■ indicates the first, whereas • the second test of the twin tests. If multiple beams have the same reinforcement configuration, their colour shading is different.

average value of $2.0f_{ctm}$, which is consistent with the assumption for elastic strains in tension chords [23]. For the bond shear stress of the orthogonal reinforcing bars of the beams with diagonal reinforcement, the experimental values are lower than this assumption. Hence, a reduced effective mean bond shear stress of $1.4f_{ctm}$ is deemed to be more representative of the real stresses. The consideration of $1.4f_{ctm}$ as an initial bond assumption would result in slightly lower measured effective bond shear stresses (8% and 11% lower bond stresses for the horizontal and vertical reinforcement, respectively) which do not change the previous interpretations.

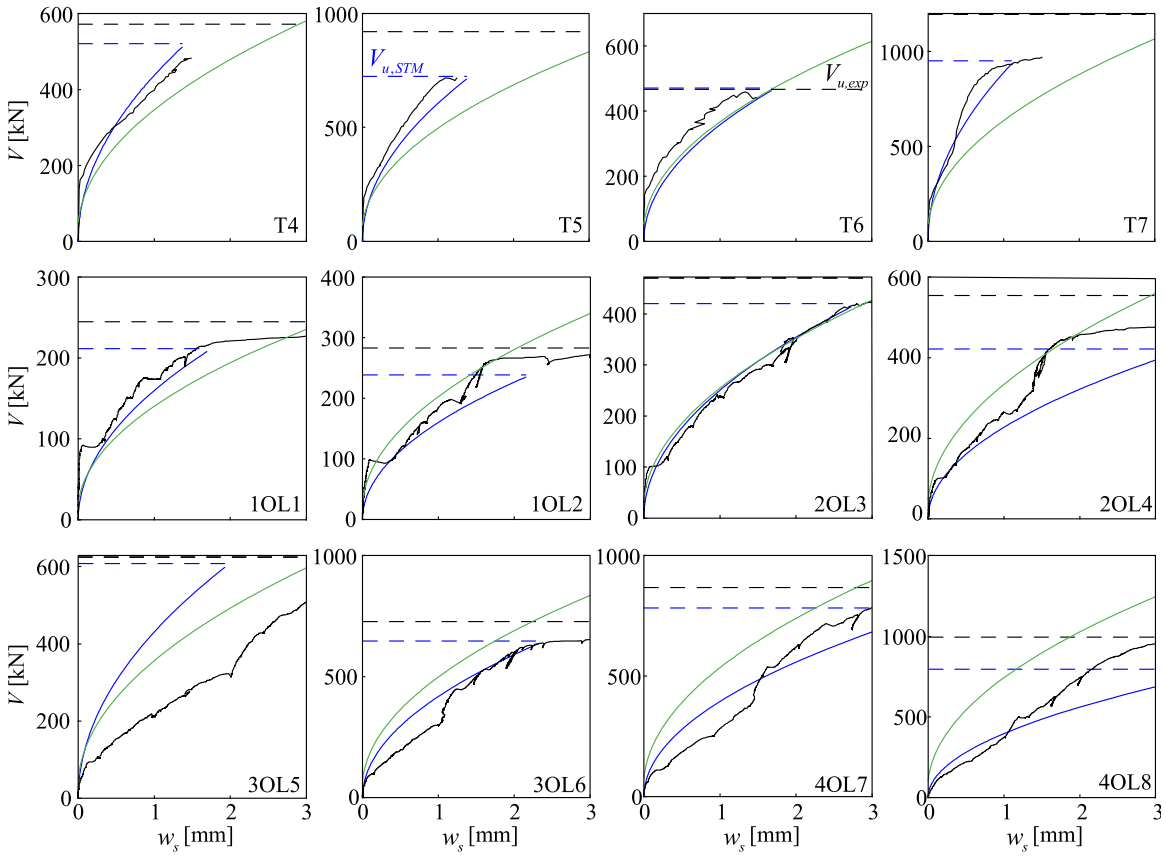

Fig. 17. Prediction of crack width at the reinforcement (in blue) compared to experimental values (in black) of the tests by Zhu et al. [11] (top row) and Rajapakse et al. [12,22] (bottom two rows). The dashed line indicates the ultimate load from the experiments (in black) and from the ULS prediction (Mata-Falcón et al. [7], in blue). The green curves represent the predictions using the compatibility-aided strut-and-tie model by Zhu et al. [11].

4.3. Differences in SLS and ULS behaviour

The load factors α_i defined in Eqs. (5), (6) and (7) characterise the strut-and-tie model at ULS (Fig. 13a), which assumes that both the diagonal and horizontal reinforcement yield. During serviceability, the concrete and reinforcement remain in the elastic range. Hence, it would not be correct to account for the plastic redistributions that the strut-and-tie model for ULS implies. The stress fields during SLS differ significantly from those during ULS. For beams with a diagonal reinforcing bar, the observations in Section 3.3 show that the load-bearing behaviour changed during the load history: at service loads (between 0.3 and $0.6V_u$), the diagonal reinforcement carried proportionally higher loads than when approaching the ultimate load, meaning that the ratio X at ULS is larger than at SLS. To account for these and other differences between serviceability and ultimate load schemes, the load factors α_V and α_H that characterise the orthogonal model at failure are amplified with the empirical factors κ_V and κ_H (see Eq. (4) and Fig. 13b) that are calibrated next.

The experimental load factors $\alpha_{i,exp}$ are defined as the average forces in the vertical and horizontal, respectively, reinforcing bars ($F_{s,i}$) divided by the proportion of the load carried by the mechanism activating the orthogonal reinforcement ($V - F_{s,D}\sin(\beta_D)$) over the range of service loads (between 0.3 and $0.6V_u$). Whereas the experimental ratio X_{exp} is the average of $1- F_{s,D}\sin(\beta_D)/V$ over the same range. The forces carried by the orthogonal reinforcement are determined as described in Section 3.3 with the measured strains. Table 4 compares these experimental load factors at SLS ($\alpha_{i,exp}$) to the load factors provided by the ULS strut-and-tie model ($\alpha_{i,ULS}$) from Eqs. (5) and (6). Due to measurement uncertainties, the results in Table 4 should be interpreted with care, particularly for the beams where the diagonal reinforcement carried most of the load (DEB-2.5 and DEB-2.6), in which the determination of X_{exp} is very uncertain and which leads to high scatter between twin tests without any physical meaning. For all beams with orthogonal reinforcement only, $\alpha_{V,exp}$ is on average 43% (standard deviation of 36%) larger than $\alpha_{V,ULS}$, while $\alpha_{H,exp}$ is on average 42% (standard deviation of 22%) larger than $\alpha_{H,ULS}$. This experimental observation supports the introduction of empirical factors $\kappa_i = 1.4$ for $i = H, V$ to amplify the load factors α_i for serviceability, see also Fig. 13c. For simplicity, the empirical factors for both vertical and horizontal reinforcement and for beams with or without diagonal reinforcement are taken as equal. As already discussed, no amplification factor needs to be applied to the diagonal load factor. The empirical amplification factors of the orthogonal reinforcement increase the amount of load carried by the diagonal reinforcement (1-X) at SLS when imposing crack kinematic compatibility Eqs. (9) and (11). The ratio (1-X) predicted by the model for SLS is marked in red in Fig. 9, showing a good agreement with the experimental observations.

Table 4 lists the load factors and ratio X measured in the experiments at serviceability, as well as the predictions with the strut-and-tie models for ULS and SLS with the mean and coefficient of variation for DEB-1.X, DEB-2.X and all specimens. Due to the above-mentioned uncertainties in the tests of beams DEB-2.5 and DEB-2.6, their values were excluded from the statistical summary. For the beams without diagonal reinforcement (DEB-1.X), the load factors at SLS are generally well predicted with an average error of 2% for α_V and 8% for α_H, respectively. As both beams DEB-2.5 and DEB-2.6 had a significant amount of diagonal reinforcement (Layouts D3 and D4.1), the load factor predictions of Beams DEB-2.5 and DEB-2.6 were largely underestimated, which could be caused by their large amount of diagonal reinforcement (Layouts D3 and D4.1) and resulted in an overprediction of the ratio X. For the remaining beams with additional diagonal reinforcement, the load factors were

underestimated by 28% for α_V and 43% for α_H, respectively, whereas the fraction of the load V carried by the diagonal reinforcement (1-X) was on average underpredicted by 12%.

5. Experimental validation

The extended strut-and-tie model for service loads is validated by experimental verification, firstly on the results presented in this study and secondly on experiments by other authors.

5.1. Model comparison with own experiments

Fig. 15 shows the predictions of the maximum crack widths w_{max} (in blue) compared with the experimental measurements presented in this experimental campaign (in black). The predicted crack behaviour up to the onset of yielding of the reinforcement coincides reasonably well, both for specimens with and without diagonal reinforcement. After yielding, the beam undergoes plastic redistributions which are consistent with the typical assumptions of a strut-and-tie model. However, this violates the underlying assumption of elastic material behaviour of the developed serviceability strut-and-tie model, which results in significant discrepancies between the estimations and the measurements.

The predictions of the compatibility-aided strut-and-tie model developed by Zhu et al. [11] are also presented in the Fig. 15 (in green). This model was empirically fitted for a reduced set of experimental data. Hence, while for some experiments with orthogonal reinforcement the predictions are reasonable, the model overestimates very significantly the crack widths in beams with diagonal reinforcement or with over-dimensioned horizontal reinforcement (Beams DEB-1.3 and DEB-2.6).

5.2. Model comparison with experiments of other authors

Although there exists a vast amount of data on ultimate loads for dapped-end beams including sufficient information on material properties, geometry and reinforcement configurations, the information on the crack behaviour is very scarce in the literature. When some information is available, it is usually a crack width, the location of which may not be defined, or the deformation of the dapped end at discrete loads approaching ultimate. Only the following three studies were found to have well-documented information about the crack behaviour of dapped ends: Herzinger [9], Zhu et al. [11] and Rajapakse et al. [12,22]. All three studies used linear voltage displacement transducers (LVDTs) to measure the crack widths. In all cases, the LVDT was placed close to the point where the main crack intersected the dapped-end reinforcement (i.e. where w_s was measured, as shown in Fig. 4). Based on the complexity of the crack patterns measured in this study (see Section 3.2), it cannot be ruled out that more than one crack was measured in these three studies when using LVDTs. To compare these measurements, the crack width was predicted using Eq. (11), i.e. without accounting for the increase of the width within the cover.

Herzinger [9] performed twin tests of dapped-end beams with four main series (A, B, C and D). Fig. 16 shows the comparison of the continuously predicted maximum crack width and the discrete points measured at different loads. Series A and B only contain specimen with orthogonal reinforcement with $A_{s,H}/A_{s,V} \approx 1.5$ and 1.4, and $f_{y,H}/f_{y,V} \approx 1.17$ and 1.74. Whereas Series C and D include additional diagonal reinforcement, and for each two reinforcement configurations were investigated (DE-X-1.0 and DE-X*-1.0). If two specimens were cast for one configuration, the lighter colour shows the second specimen (DE-Xu-1.0). Series B included different distances between load introduction and support: 1000 mm in black and 500 mm in blue. The proposed model yields reasonable predictions. The estimations lie on the unsafe side only for Series B and configuration DE-Du-1.0. The experimentally measured crack widths of Series A are much lower than Series B, although they reach similar ultimate loads, which might explain their stark differences.

Zhu et al. [11] conducted four twin tests of dapped-end beams, two with orthogonal reinforcement only (T4 and T6) and two with additional diagonal reinforcement (T5 and T7). The crack width measurements were averaged over six LVDT measurements, three for each dapped end. The crack width predictions from the model and the measurements are shown in Fig. 17 (top row). In this case, the crack widths are well predicted and tend to be conservative, particularly for T5 and T6. The proposed calculation of the crack width, which relies on a mechanically sound strut-and-tie model and empirical parameters to account for the conditions at service loads, provides even better predictions than the compatibility-aided strut-and-tie model by Zhu et al. [11] that was fitted to these experiments. This result highlights the ability of the model to predict configurations that are very different from those used to calibrate its empirical parameters (Sections 4.2 and 4.3).

Lastly, Rajapakse et al. [12,22] conducted eight dapped-end tests with only orthogonal reinforcement (XOLY). The model predictions of the crack widths compared with the measurements at the reinforcement are shown in Fig. 17 (bottom two rows). This experimental campaign varied the reinforcement ratio and the ratio between the horizontal and the hanger reinforcement (for each reinforcement ratio, one dapped end test was conducted with $A_{s,H}/A_{s,V} \approx$ 1.3..1.5 and one with 0.70..0.75). For beams with low amounts of reinforcement (1OL1, 1OL2, 2OL3 and 2OL4), the model predicts the crack width very well, particularly in the range of serviceability (up to 1 mm). The reinforcement contents of those beams were in the range of the reinforcement contents explored in the experimental campaign presented in this paper. However, for the beams with higher reinforcement ratios (3OL5, 3OL6, 4OL7 and 4OL8), the model underestimates the crack width at service loads, particularly for Beam 3OL5.

These results indicate that the effect of restrained shrinkage, which depends on the amount of reinforcement, might not be properly captured in heavily reinforced dapped ends when using the effective bond shear stresses that have been calibrated in this study using moderately reinforced dapped ends. Moreover, recent publications have shown that the bond shear stress decreases as the diameter of the reinforcing bar increases [34,35], which should be considered when accounting for the crack behaviour of dapped-end beams with larger diameters [22]. Therefore, it is likely that the effective bond estimation conducted in Section 4.2 based on the experiments of this study is not conservative for heavily reinforced dapped ends. Further experimental evidence is required to investigate the bond strength and the impact of restrained shrinkage in dapped ends with a wide range of reinforcement amounts.

6. Conclusions

The formation of a diagonal crack at the re-entrant corner of dapped-end beams at low loads tends to induce corrosion and stress concentration, which can ultimately compromise the safety of the joint. The behaviour of these cracks located in a highly disturbed region of the structure is not yet well understood and differs significantly from the behaviour of distributed cracks due to bending or tensile actions. This lack of understanding can be partly explained by the limited experimental evidence on crack widths in dapped ends, which contrasts with the extensive information on their ultimate behaviour. Furthermore, the very few analytical models proposed in recent years to calculate crack widths in dapped ends [11,21,22] differ significantly in the bond shear stress developed by the dapped-end reinforcement. In order to improve the knowledge of this phenomenon, this paper presents an experimental

investigation of 28 dapped-end tests, in which the crack and bond behaviour under service loads was analysed in detail. Based on these observations, a model is proposed for evaluating the width of corner cracks at service loads. In this model, reinforcement strains are calculated using an extension of an existing strut-and-tie model for ultimate to service loads. The following conclusions are drawn:

1. The mean value of the diagonal crack width at service loads (40% of the ultimate load) in this test campaign was 0.40 mm, where the specimens with diagonal reinforcement showed slightly better crack control. This crack width is above the limits for durability requirements. Therefore, crack width control is critical in the design of most dapped-end beams, even those with diagonal reinforcement.
2. The refined digital image correlation analysis of the crack behaviour around the re-entrant corner showed that the diagonal crack branches out sometimes before it crosses the dapped-end reinforcement. While the local width of each crack branch crossing the reinforcement is critical for durability, the superposed width of the crack branches is more representative for quantifying the overall mechanical behaviour and reinforcement activation.
3. The diagonal crack forming at the re-entrant corner is isolated until its width reaches a value of approximately 0.30 mm. Secondary cracks will subsequently form and modify the behaviour of the main crack, but their influence can be disregarded for serviceability checks.
4. An effective bond behaviour of the dapped-end reinforcement was estimated from the measured crack widths and reinforcement strains, assuming a pull-out mechanism with constant bond shear stresses on both crack sides. The effective bond includes the effect of restrained shrinkage. For the tests without dapped-end diagonal reinforcement, an effective bond value of $2.0f_{ctm}$ was found on average to represent the experimental serviceability results well. This value is consistent with the assumption of elastic strains in tension chords. In the beams with diagonal reinforcement, the orthogonal reinforcing bars showed a lower effective bond value ($1.4f_{ctm}$), while the conventional bond value ($2.0f_{ctm}$) is representative for the effective bond of diagonal reinforcing bars.
5. The crack width can be calculated by relying on the previous bond assumptions and using a strut-and-tie model to estimate the dapped-end reinforcement strains at service loads. A strut-and-tie model proposed by the authors was modified with empirical factors to account for the differences between the serviceability and ultimate load-bearing behaviour.
6. The crack widths calculated with the proposed model agreed satisfactorily well with the experimental measurements presented in this paper (i.e. for the tests from which the average bond shear stresses were fitted to). For tests performed by other authors, the crack width predictions also show little scatter, except for beams with large reinforcement diameters (20 mm or larger) and amounts where the proposed bond shear stress seems to be excessive.
7. Further research is required to understand (i) the bond behaviour of dapped-end reinforcing bars with large diameters, (ii) the role of shrinkage in the crack behaviour of dapped-ends and (iii) the effect of secondary crack to estimate crack widths beyond the serviceability range.

CRediT authorship contribution statement

Jaime Mata-Falcón: Conceptualisation, Methodology, Investigation, Writing – original draft, Supervision. **Karin L. Yu;** Methodology, Software, Validation, Data curation, Writing – original draft, Visualisation. **Luis Pallarés Rubio:** Project administration, Funding acquisition, Writing – review & editing. **Pedro Miguel Sosa:** Project administration, Funding acquisition, Writing – review & editing.

Declaration of Competing Interest

The authors declare that they have no known competing financial interests or personal relationships that could have appeared to influence the work reported in this paper.

Data availability

The data that support the findings of this study are available from the corresponding author upon reasonable request.

Acknowledgements

The authors wish to thank the Spanish Ministry of Science and Innovation for funding Project BIA2009–11369 and for FPI fellowship BES-2010–030353 received by Jaime Mata-Falcón. A special thanks for supporting the research goes to Prof. Dr. Walter Kaufmann (ETH Zurich).

Appendix A: Approximation of the development of the governing crack

This appendix describes the derivation of a mechanical model used to approximate the ratio μ_w of the crack width at the reinforcement location (w_s) over the maximum crack width (w_{max}) at the re-entrant corner of the dapped end. Since the distance between these two crack widths is defined by the concrete cover which for usual member sizes is small compared to the member size, the crack width at the re-entrant corner is assumed to depend linearly on the crack width at the reinforcement crossing during serviceability, resulting in a linear crack. This model is equivalent to a fully cracked elastic cross-sectional analysis in a beam. Since the Bernoulli hypothesis that states that plain sections remain plain does not hold for the dapped end or any discontinuity region, an equivalent nonplanar section (bilinear) perpendicular to the elastic trajectories is considered, in which the strains are assumed to be distributed linearly.

It is assumed that (i) there is no horizontal reaction force ($H = 0$), (ii) the behaviour of concrete and steel is linear elastic and (iii) the crack opens linearly. Fig. 18 shows the notations used for the derivation. For this model, the Young's modulus of concrete is approximated by Eq. (A 1).

$$E_c = 10,000\sqrt[3]{f_c + 8} \tag{A 1}$$

where f_c is the concrete compressive strength in MPa.

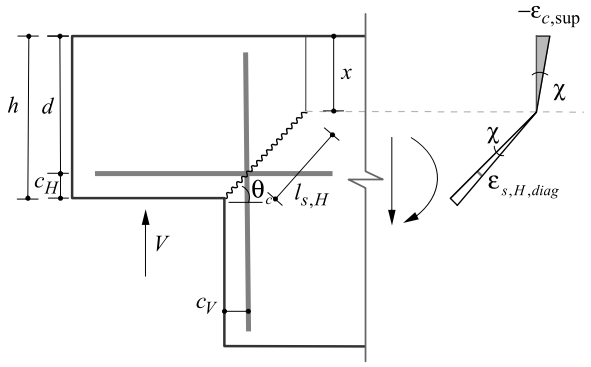

Fig 18. Mechanical model to estimate the crack width length.

.

The factor μ_w is determined as follows, where h is the height, d the static height of the nib and x the compression depth.

$$\mu_w = \frac{w_s}{w_{\max}} = \frac{d-x}{h-x} \tag{A 2}$$

The main unknown is the concrete compression depth x. $l_{s,h}$ is the length of the crack until the reinforcement crossing and can be derived as follows, where θ_c is the crack angle.

$$l_{s,H} = \frac{d-x}{\sin(\theta_c)} \tag{A 3}$$

The curvature χ at the concrete compression zone and of the main crack are assumed to be equal, where $\varepsilon_{c,\sup}$ is the maximum concrete compressive strain:

$$\chi = \frac{\varepsilon_{c,\sup}}{x} = \frac{\varepsilon_{s,H,diag}}{l_{s,H}} \tag{A 4}$$

The concrete force F_c is then given by the following equation, where b is the width of the element:

$$F_c = \frac{1}{2} \cdot x \cdot b \cdot E_c \cdot \varepsilon_{c,\sup} \tag{A 5}$$

The steel forces $F_{s,i}$ are obtained through:

$$F_{s,i} = A_{si} \cdot E_s \cdot \varepsilon_{s,i}, \quad \text{for } i = H, D \tag{A 6}$$

For the global system it is assumed that all reinforcing bars cross each other at the same point at the re-entrant corner, thus the horizontal projection of the diagonal strain $\varepsilon_{s,H,diag}$ is equal to the projections of the horizontal and vertical reinforcement strains.

$$\varepsilon_{s,H,diag} = \varepsilon_{s,H} \cdot \cos^2(\theta_c) = \varepsilon_{s,V} \cdot \sin^2(\theta_c) \tag{A 7}$$

For the beams with orthogonal reinforcement only, the horizontal equilibrium is given by $F_c = F_{s,H}$. The equation can then be solved for x^2.

$$x^2 = \frac{2 \cdot A_{s,H} \cdot E_s}{E_c \cdot b \cdot \cos^2(\theta_c)} \cdot \frac{d-x}{\sin(\theta_c)} \tag{A 8}$$

For the beams with additional diagonal reinforcement, the horizontal equilibrium includes a term for the diagonal reinforcing bars $F_c = F_{s,H} + F_{s,D} \cdot \cos(\beta_D)$:

$$\varepsilon_{s,D} = \varepsilon_{s,H} \cdot \cos^2(\beta_D) + \varepsilon_{s,V} \cdot \sin^2(\beta_D) \tag{A 9}$$

Table 5
Derived factor μ_w for each test of this study and other studies, assuming $\theta_c = 45°$.

Specimen	DEB-1.1	DEB-1.2	DEB-1.3	DEB-1.4	DEB-1.5	DEB-1.6	DEB-1.7	DEB-1.8	DEB-1.9
$\mu_w = w_s/w_{\max}$ [-]	0.764	0.780	0.763	0.763	0.781	0.724	0.754	0.745	0.767
Specimen	DEB-2.1	DEB-2.2	DEB-2.3	DEB-2.4	DEB-2.5	DEB-2.6			
$\mu_w = w_s/w_{\max}$ [-]	0.768	0.737	0.751	0.743	0.751	0.703			
Specimen[9]	DE-A-0.5	DE-B-1.0	DE-B-0.5	DE-C-1.0	DE-C*-1.0	DE-Cu*-1.0	DE-D-1.0	DE-D*-1.0	DE-Du-1.0
$\mu_w = w_s/w_{\max}$ [-]	0.772	0.777	0.776	0.802	0.803	0.802	0.805	0.815	0.805
Specimen[9,11]	DE-Du*-1.0	T4	T5	T6	T7				
$\mu_w = w_s/w_{\max}$ [-]	0.815	0.777	0.776	0.795	0.768				
Specimen[12,22]	1OL1	1OL2	2OL3	2OL4	3OL5	3OL6	4OL7	4OL8	
$\mu_w = w_s/w_{\max}$ [-]	0.897	0.897	0.888	0.888	0.877	0.877	0.865	0.865	

$$x^2 = \frac{2 \cdot E_s}{b \cdot E_c} \cdot \left(\frac{A_{s,H}}{\cos^2(\theta_c)} + A_{s,D} \cdot \cos(\beta_D) \cdot \left(\frac{\cos^2(\beta_D)}{\cos^2(\theta_c)} + \frac{\sin^2(\beta_D)}{\sin^2(\theta_c)} \right) \right) \cdot \frac{d - x}{\sin(\theta_c)} \quad \text{(A 10)}$$

Eqs. (A 8) and (A 9) can be solved for x using the quadratic formula, where the positive root is taken. Table 5 lists the obtained factor μ_w for each test.

References

[1] Desnerck P., Lees J.M., Valerio P., Loudon N., Morley C.T. Inspection of RC half-joint bridges in England: analysis of current practice. Proceedings of the Institution of Civil Engineers - Bridge Engineering 2018;171:290–302. https://doi.org/10.1680/jbren.18.00004.

[2] EN 1992–1-1. Eurocode 2: Design of concrete structures - Part 1–1: General rules and rules for buildings 2010.

[3] European Committee for Standardization. Eurocode 2: Design of concrete structures - Part 2: Bridges 2011.

[4] Johnson P., Couture A., Nicolet R. Report of the Commission of inquiry into the collapse of a portion of the de la Concorde overpass. Québec, Canada: 2007.

[5] Bazzucchi F, Restuccia L, Ferro G. Considerations over the Italian road bridge infrastructure safety after the Polcevera viaduct collapse: past errors and future perspectives. Frat Ed Integrità Strutt 2018;12:400–21. https://doi.org/10.3221/IGF-ESIS.46.37.

[6] Desnerck P, Lees JM, Morley CT. Impact of the reinforcement layout on the load capacity of reinforced concrete half-joints. Eng Struct 2016;127:227–39. https://doi.org/10.1016/j.engstruct.2016.08.061.

[7] Mata-Falcón J, Pallarés L, Miguel PF. Proposal and experimental validation of simplified strut-and-tie models on dapped-end beams. Eng Struct 2019;183:594–609. https://doi.org/10.1016/j.engstruct.2019.01.010.

[8] Desnerck P, Lees JM, Morley CT. Strut-and-tie models for deteriorated reinforced concrete half-joints. Eng Struct 2018;161:41–54. https://doi.org/10.1016/j.engstruct.2018.01.013.

[9] Herzinger R. Stud reinforcement in dapped ends of concrete beams. PhD Thesis Univ Calg 2008.

[10] Cook WD, Mitchell D. Studies of disturbed regions near discontinuities in reinforced concrete members. Acids Struct J 1988;85:206–16.

[11] Zhu RR, Wanichakorn W, Hsu TT, Vogel J. Crack width prediction using compatibility-aided strut-and-tie model. Acids Struct J 2003;100:413–21.

[12] Rajapakse C, Degée H, Mihaylov B. Investigation of shear and flexural failures of dapped-end connections with orthogonal reinforcement. Eng Struct 2022;260:114233. https://doi.org/10.1016/j.engstruct.2022.114233.

[13] Rajapakse C, Degée H, Mihaylov B. Experimental investigation of dapped ends with diagonal reinforcement. Acids Struct J 2024:121. https://doi.org/10.14359/51740710.

[14] Nagrodzka-Godycka K, Piotrkowski P. Experimental study of dapped-end beams subjected to inclined load. SJ 2012:109. https://doi.org/10.14359/51683489.

[15] Schlaich J, Schäfer K, Jennewein M. Toward a consistent design of structural concrete. PCI J 1987;32:74–150. https://doi.org/10.15554/pcij.05011987.74.150.

[16] Lourenço MS, Fernández Ruiz M, Blaauwendraad J, Bousias S, Hoang LC, Mata-Falcón J, et al. Design and assessment of concrete structures with strut-and-tie models and stress fields: From simple calculations to detailed numerical analysis. Struct Concr 2023. https://doi.org/10.1002/suco.202200647.

[17] Rajapakse C, Degée H, Mihaylov B. Assessment of failure along re-entrant corner cracks in existing RC dapped-end connections. Struct Eng Int 2021;31:216–26. https://doi.org/10.1080/10168664.2021.1878975.

[18] Menichini G, Gusella F, Orlando M. Methods for evaluating the ultimate capacity of existing RC half-joints. Eng Struct 2024;299:117087. https://doi.org/10.1016/j.engstruct.2023.117087.

[19] Belletti B, Calcavecchia B, Ferretti D, Ravasini S. Capacity assessment of uncorroded and corroded dapped-end beams by NLFE and strut-and-tie based methods. Struct Concr 2024;25:1275–304. https://doi.org/10.1002/suco.202301020.

[20] Ajina J.M. Effect of Steel Fibers on Precast Dapped-end Beam Connections. MSc thesis. South Dakota State University, 1986.

[21] Mihaylov BI. Model for rapid evaluation of corner crack widths in reinforced concrete dapped-end connections. Eng Struct 2024;303:117497. https://doi.org/10.1016/j.engstruct.2024.117497.

[22] Rajapakse C. Behaviour and Modelling of Reinforced Concrete Dapped-End Connections. Doctoral thesis. Université de Liège; 2023.

[23] Sigrist V. Zum Verformungsvermögen von Stahlbetonträgern. Doctoral dissertation. Institut für Baustatik und Konstruktion. ETH: Zürich; 1995.

[24] Mata-Falcón J. Serviceability and ultimate behaviour of dapped-end beams (In Spanish: Estudio del comportamiento en servicio y rotura de los apoyos a media madera). PhD thesis. Universitat Politècnica de València, 2015.

[25] Alvarez M. Einfluss des Verbundverhaltens auf das Verformungsvermögen von Stahlbeton. Doctoral d. ETH Zur 1998. https://doi.org/10.3929/ETHZ-A-002000033.

[26] Zhang Z. A flexible new technique for camera calibration. Pattern Anal Mach Intell 2002;22:1330–4. https://doi.org/10.1109/34.888718.

[27] Heikkila J., Silven O. A four-step camera calibration procedure with implicit image correction. Computer Vision and Pattern Recognition, 1997. Proceedings., 1997 IEEE Computer Society Conference on, San Juan, Puerto Rico: 2002, p. 1106–1112.

[28] Correlated Solutions. Vic-2D 6.2 Manual 2020.

[29] Mata-Falcón J, Haefliger S, Lee M, Galkovski T, Gehri N. Combined application of distributed fibre optical and digital image correlation measurements to structural concrete experiments. Eng Struct 2020;225:111309. https://doi.org/10.1016/j.engstruct.2020.111309.

[30] Gehri N, Mata-Falcón J, Kaufmann W. Automated crack detection and measurement based on digital image correlation. Constr Build Mater 2020;256:119383. https://doi.org/10.1016/j.conbuildmat.2020.119383.

[31] Gehri N, Mata-Falcón J, Kaufmann W. Refined extraction of crack characteristics in Large-scale concrete experiments based on digital image correlation. Eng Struct 2022;251:113486. https://doi.org/10.1016/j.engstruct.2021.113486.

[32] Cook WD. Studies of reinforced concrete regions near discontinuities. PhD Thesis McGill Univ 1987.

[33] SIA 262 Concrete Structures. Zürich: Schweizerischer Ingenieur- und Architekten-Verein; 2013.

[34] Galkovski T, Mata-Falcón J, Kaufmann W. Experimental investigation of bond and crack behaviour of reinforced concrete ties using distributed fibre optical sensing and digital image correlation. Eng Struct 2023;292:116467. https://doi.org/10.1016/j.engstruct.2023.116467.

[35] Galkovski T, Mata-Falcón J, Kaufmann W. Stress field model for bond in reinforced concrete ties. Eng Struct 2023;294:116759. https://doi.org/10.1016/j.engstruct.2023.116759.